

CHARACTERIZATION OF THE KOI-94 SYSTEM WITH TRANSIT TIMING VARIATION ANALYSIS: IMPLICATION FOR THE PLANET-PLANET ECLIPSE

KENTO MASUDA,¹ TERUYUKI HIRANO,² ATSUSHI TARUYA,^{1,3,4} MAKIKO NAGASAWA,⁵ AND YASUSHI SUTO^{1,3,6}

Accepted 2013 October 21

ABSTRACT

The KOI-94 system is a closely-packed, multi-transiting planetary system discovered by the *Kepler* space telescope. It is known as the first system that exhibited a rare event called a “planet-planet eclipse (PPE),” in which two planets partially overlap with each other in their double-transit phase. In this paper, we constrain the parameters of the KOI-94 system with an analysis of the transit timing variations (TTVs). Such constraints are independent of the radial velocity (RV) analysis recently performed by Weiss and coworkers, and valuable in examining the reliability of the parameter estimate using TTVs. We numerically fit the observed TTVs of KOI-94c, KOI-94d, and KOI-94e for their masses, eccentricities, and longitudes of periastrons, and obtain the best-fit parameters including $m_c = 9.4_{-2.1}^{+2.4} M_{\oplus}$, $m_d = 52.1_{-7.1}^{+6.9} M_{\oplus}$, $m_e = 13.0_{-2.1}^{+2.5} M_{\oplus}$, and $e \lesssim 0.1$ for all the three planets. While these values are mostly in agreement with the RV result, the mass of KOI-94d estimated from the TTV is significantly smaller than the RV value $m_d = 106 \pm 11 M_{\oplus}$. In addition, we find that the TTV of the outermost planet KOI-94e is not well reproduced in the current modeling. We also present analytic modeling of the PPE and derive a simple formula to reconstruct the mutual inclination of the two planets from the observed height, central time, and duration of the brightening caused by the PPE. Based on this model, the implication of the results of TTV analysis for the time of the next PPE is discussed.

Subject headings: planets and satellites: individual (KOI-94, KIC 6462863, Kepler-89) – techniques: photometric

1. INTRODUCTION

The Kepler Object of Interest (KOI) 94 system is a multi-transiting planetary system discovered by the *Kepler* space telescope (Borucki et al. 2011; Batalha et al. 2013), consisting of four transiting planets with periods of about 3.7 (KOI-94b), 10 (KOI-94c), 22 (KOI-94d), and 54 (KOI-94e) days (Figure 1). For the largest planet KOI-94d, Hirano et al. (2012) observed the Rossiter-McLaughlin effect (Rossiter 1924; McLaughlin 1924; Queloz et al. 2000; Ohta et al. 2005; Winn et al. 2005; Hirano et al. 2011) for the first time in a multi-transiting system. They found $\lambda = -6_{-11}^{+13}$ deg, showing that the orbital axis of this planet is aligned with the stellar spin axis (this result was later confirmed by Albrecht et al. (2013), who obtained $\lambda = -11 \pm 11$ deg). Furthermore, the KOI-94 system is the first and only system in which a rare mutual event called a “planet-planet eclipse” (hereafter PPE) was identified; in this event, two planets transit simultaneously and partially

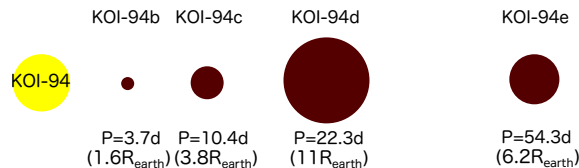


FIG. 1.— Schematic illustration of the KOI-94 system. Planetary radii are calculated from the planet-to-star radius ratio, stellar density obtained from the transit light curves, and spectroscopic stellar mass $M_{\star} = 1.25 M_{\odot}$ (Hirano et al. 2012).

overlap with each other on the stellar disk as seen from our line of sight. By analyzing the light curve of the PPE caused by KOI-94d and KOI-94e, Hirano et al. (2012) concluded that the orbital planes of these two planets are also well aligned within 2 degrees. In this system, therefore, the stellar spin axis and the orbital axes of the two planets are all aligned. If their close-in orbits are due to planetary migration (e.g. Lubow & Ida 2011), this result suggests that they have experienced a quiescent disk migration (Goldreich & Tremaine 1980) rather than processes that include gravitational perturbations either by planets (e.g. Nagasawa et al. 2008; Wu & Lithwick 2011; Naoz et al. 2011) or stars (e.g. Wu & Murray 2003). Other processes that tilt the stellar spin axis relative to orbital axes of planets (e.g. Bate et al. 2010; Lai et al. 2011; Rogers et al. 2012; Batygin 2012) are also excluded, provided that the orbital planes of the multiple transiting planets trace the original protoplanetary disk from which they formed. For these reasons, the KOI-94 system is an important test bed that provides a clue to understand the formation process of closely-packed multi-transiting planetary systems, and hence deserves to be characterized in detail.

masuda@utap.phys.s.u-tokyo.ac.jp

¹ Department of Physics, The University of Tokyo, Tokyo 113-0033, Japan

² Department of Earth and Planetary Sciences, Tokyo Institute of Technology, 2-12-1 Ookayama, Meguro-ku, Tokyo 152-8551, Japan

³ Research Center for the Early Universe, Graduate School of Science, The University of Tokyo, Bunkyo-ku, Tokyo 113-0033, Japan

⁴ Yukawa Institute for Theoretical Physics, Kyoto University, Kyoto 606-8502, Japan

⁵ Interactive Research Center of Science, Tokyo Institute of Technology, 2-12-1 Ookayama, Meguro-ku, Tokyo 152-8551, Japan

⁶ Department of Astrophysical Sciences, Princeton University, Princeton, NJ 08544, USA

Recently, Weiss et al. (2013) measured the radial velocities (RVs) of KOI-94 from the W. M. Keck Observatory, and estimated the masses and eccentricities of the planets by a simultaneous fit to the observed RVs and the *Kepler* light curve. They showed that the masses of all the planets fall into the planetary regime, and especially obtained a fairly well constraint on the mass of KOI-94d ($m_d = 106 \pm 11 M_\oplus$). However, the masses of KOI-94c ($m_c = 15.6^{+5.7}_{-15.6} M_\oplus$) and KOI-94e ($m_e = 35^{+18}_{-28} M_\oplus$) are weakly constrained because of the marginal detections of their RV signals. In addition, the best-fit eccentricity of KOI-94c ($e_c = 0.43 \pm 0.23$) is suspiciously large in light of the long-term stability of the system, as pointed out in their paper. Hence additional RV observations are definitely important, but transit timing variations (TTVs, Holman & Murray 2005; Agol et al. 2005) can also be used to improve these estimates in such a multi-transiting system like KOI-94 (e.g. TTV analysis in the Kepler-11 system by Lissauer et al. 2011). Moreover, in the KOI-94 system the orbital parameters are exceptionally well constrained by the observations of the Rossiter-McLaughlin effect and the PPE; this makes the KOI-94 system an ideal case to evaluate the reliability of the parameter estimates by TTVs in comparison to RVs.

Apart from such characterization of the KOI-94 system, the PPE itself is a unique phenomenon that is worth studying in a more general context. If this event is observed in the future transit observations, it can be used to precisely constrain the relative angular momentum of the planets, which is closely related to their orbital evolution processes. In fact, this phenomenon had been theoretically predicted before by Ragozzine & Holman (2010) (see also Rabus et al. 2009) as an “overlapping double transit,” and they emphasized its role in constraining the relative nodal angle of the planets. However, neither the analytic formulation that clarifies the physical picture of this phenomenon, nor the discussion about how gravitational interactions among the planets affect the PPE, has been presented so far.

In this paper, we investigate the constraints on masses and eccentricities of KOI-94c, KOI-94d, and KOI-94e based on the direct numerical analysis of their TTV signals. We also construct an analytic model of the PPE, and discuss how the gravitational interaction affects the occurrence of the next PPE based on the model and the result of TTV analysis.

The plan of this paper is as follows. First, we perform an intensive TTV analysis in Section 2. We discuss the constraints on transit parameters based on the phase-folded transit light curves, and those on the mass, eccentricity, and longitude of periastron based on the numerical fit to the observed TTV signals. Then in Section 3, we present an analytic description of the PPE which elucidates how the height, duration, and central time of the brightening caused by the overlap are related to the orbital parameters. Based on this formulation, we provide a general procedure for constraining the orbits of the overlapping planets in Section 4. Here we also discuss a simple prediction of the next PPE on the basis of a two-body problem. Finally, based on the analytic model of the PPE and the result of TTV analysis, we show in Section 5 how the gravitational interaction among the planets affects the occurrence of the next PPE in the

KOI-94 system, referring to the difference from the two-body prediction. Section 6 summarizes the paper. The results on the properties of the KOI-94 system are all in Section 2, and so the readers who are only interested in the TTV analysis can skip Sections 3 to 5, where we mainly discuss the PPE.

2. ANALYSIS OF THE PHOTOMETRIC LIGHT CURVES

In this section, we report the analysis of photometric light curves of KOI-94 taken by *Kepler*. We determine the orbital phases, scaled semi-major axes, scaled planetary radii, and inclinations of KOI-94c, KOI-94d, and KOI-94e from the phase-folded transit light curves, and estimate their masses, eccentricities, and longitudes of periastrons from their TTV signals (see Table 1). In the following analysis, we neglect the smallest and innermost planet KOI-94b, which does not affect the TTV signals of the other three, as we will see in Section 2.2.

2.1. Transit times and transit parameters

2.1.1. Data processing

We analyze the short-cadence (~ 1 min) PDCSAP (Pre-search Data Conditioned Simple Aperture Photometry) fluxes (e.g. Kinemuchi et al. 2012) from Quarters 4, 5, 8, 9, 12, and 13. We do not include the data from Quarter 1, for which only the long-cadence data is available. Since these light curves exhibit the long-term trends that affect the baseline of the transit, we remove those trends in the following manner. First, data points within ± 1 day of every transit caused by KOI-94c, KOI-94d, or KOI-94e are extracted and each set of the data is fitted with a fifth-order polynomial, masking out the points during the transit. Then we calculate the standard deviation of each fit, remove outliers exceeding 5σ , and fit the data again with the fifth-order polynomial. This process is iterated until all the 5σ outliers are removed. Finally, all the data points in each chunk (including those during the transit) are divided by the best-fit polynomial to yield a detrended and normalized transit light curve. In our analysis of the TTV, we exclude the transits whose ingress or egress is not completely observed due to the data cadence of *Kepler*. We also exclude the “double-transit” events, during which two planets transit the stellar disk at the same time. As an exception, the double transit of KOI-94d and KOI-94e around BJD = 2454211.5 (in which a PPE was observed) is included in our analysis; in this case the ingresses and egresses of both transits are clearly seen because of their close mid-transit times. The above criteria leave us with 44, 21, and 8 transits for KOI-94c, KOI-94d, and KOI-94e, respectively.

2.1.2. Transit parameters

Before analyzing the TTV signals, we revise the transit parameters of KOI-94c, KOI-94d, and KOI-94e obtained by the Kepler team (Table 2) so that they are consistent with the light curves obtained in Section 2.1.1. Here we first use the parameters publicized by the Kepler team to phase-fold the observed transit light curves, and then refit those phase curves to obtain the revised transit parameters.

TABLE 1
 DEFINITIONS OF THE PARAMETERS DERIVED IN THIS PAPER.

Parameter	Definition
<i>Parameters derived from transit light curves</i>	
t_0	Time of a transit center (BJD - 2454833)
P	Orbital period
R_p/R_\star	Planet-to-star radius ratio
a/R_\star	Scaled semi-major axis
b	Impact parameter of the transit ($= a \cos i/R_\star$, i : orbital inclination)
u_1, u_2	Coefficients for the quadratic limb-darkening law
<i>Parameters derived from the PPE^a</i>	
Ω	Longitude of the ascending node
<i>Parameters derived from TTVs</i>	
m	Planetary mass
e	Orbital eccentricity
$\varpi = \omega + \Omega$	Longitude of the periastron

^aPPE can only constrain the difference of the nodal angles of KOI-94d and KOI-94e. We have no information on Ω of KOI-94c.

 TABLE 2
 PARAMETER VALUES ESTIMATED BY OTHER AUTHORS.

Parameter	KOI-94c	KOI-94d	KOI-94e
<i>Transit parameters determined by the Kepler team^a</i>			
t_0 (BJD - 2454833)	138.00718 ± 0.00093	132.74047 ± 0.00019	161.23998 ± 0.00079
P (days)	10.423707 ± 0.000026	22.343001 ± 0.000011	54.31993 ± 0.00012
a/R_\star	15.70 ± 0.37	26.10 ± 0.62	47.2 ± 1.1
R_p/R_\star	0.02544 ± 0.00012	0.06856 ± 0.00012	0.04058 ± 0.00013
b	0.019 ± 0.048	0.305 ± 0.014	0.387 ± 0.014
<i>Parameters determined by Hirano et al. (2012)</i>			
Ω (deg) ^b	-6^{+13}_{-11}	–	-5^{+13}_{-11}
u_1		0.10 ± 0.06	
u_2		0.61 ± 0.08	
<i>Parameters determined by Weiss et al. (2013)</i>			
m (M_\oplus)	$15.6^{+5.7}_{-15.6}$	106 ± 11	35^{+18}_{-28}
e	0.43 ± 0.23	0.022 ± 0.038	0.019 ± 0.23

^aData from MAST archive <http://archive.stsci.edu/kepler/>

^bIn this paper, we define the reference direction so that the spin-orbit angle λ measured by the Rossiter-McLaughlin effect be equal to Ω for the orbital inclination in the range $[0, \pi/2]$ (Fabrycky & Winn 2009). With this choice, the reference line points to the ascending node of a virtual circular orbit whose angular momentum is parallel to the stellar spin vector.

In the first step, we fit each of the detrended light curve centered at the transit (for ~ 1.7 times its duration) to obtain the times of transit centers t_c , using a Markov chain Monte Carlo (MCMC) algorithm. Here we use a light curve model by Ohta et al. (2009), and fix a/R_\star , R_p/R_\star , and b to the values obtained by the Kepler team, assuming $e = 0$. We model the limb-darkening using a quadratic law in Eq.(7) and adopt the limb-darkening coefficients u_1 and u_2 obtained by Hirano et al. (2012) (all these parameters are summarized in Table 2). Since the detrend procedure in Section 2.1.1 can remove only the out-of-transit outliers, we also exclude in-transit 5σ outliers of this fit, if any, and fit the light curve again. Using the series of t_c obtained in this way, we construct the phase-folded transit light curve for each planet.

As the second step, we fit the resulting phase-folded transit light curve for a/R_\star , R_p/R_\star , b , u_1 , and u_2 using the same light curve model as above. In this way, we obtain the revised values of the set of parameters shown in Table 3 and the corresponding best-fit light curves (Figures 2 to 4).⁷ In this fit, all the param-

eters converge well in the case of KOI-94d. In contrast, a/R_\star and b of KOI-94c and KOI-94e do not converge well moving back and forth between several local minima in a strongly correlated fashion, because they show smaller transit depths and the ingresses/egresses of their transits are less clear. For this reason, we impose an additional constraint that all the planets share the same host star: we convert the well-constrained a/R_\star for KOI-94d into stellar density ρ_\star via $\rho_\star \approx (3\pi/GP^2)(a/R_\star)^3$ (Seager & Mallén-Ornelas 2003), and calculate the corresponding values and uncertainties of a/R_\star for KOI-94c and KOI-94e. The phase curves of KOI-94c and KOI-94e are fitted with prior constraints centered on these values and with Gaussian widths of their uncertainties. With this prescription, all the parameters of KOI-94c and KOI-94e converge well. Therefore, it does not make sense here to discuss the consistency of ρ_\star calculated from the transit parameters to check the possible false positives. It

larger R_p by a fraction of $\sim c/2$, where c is the fractional contamination (e.g. Fabrycky et al. 2012), but the other parameters were consistent within 2.1σ except for a_c and a_e . These two parameters were different from those in Table 3 by $\sim 1\%$, corresponding to a slight change in the value of a_d . In this paper, we do not apply this correction because the smaller values of R_p lead to more conservative estimates for the PPE occurrence.

⁷ We also repeated the same analysis taking account of the quarter-to-quarter flux contaminations publicized by the Kepler team and available at MAST archive. As expected, we obtained

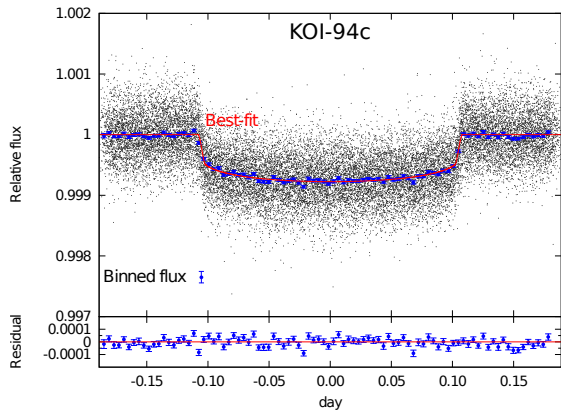


FIG. 2.— Phase-folded transit light curve of KOI-94c. The best-fit model is shown with the red solid line. Small gray dots are all the short-cadence data points. Blue points are fluxes binned to 0.1 hr bins and their error bars are calculated by $1.4826 \times$ median absolute deviation.

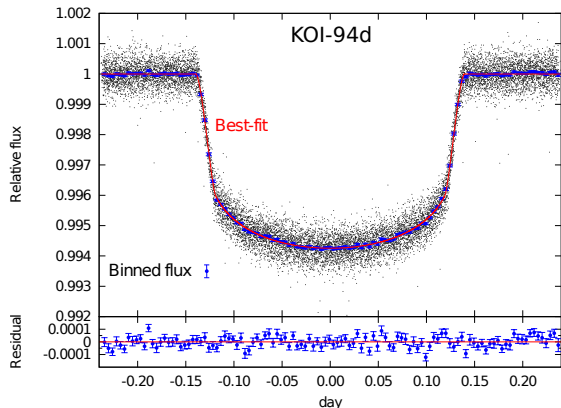


FIG. 3.— Phase-folded transit light curve of KOI-94d (same as Figure 2).

is important to note, however, that the limb-darkening coefficients for each planet obtained individually are consistent within their 1σ error bars (those obtained by Hirano et al. (2012) are different from our values because they fixed smaller R_p/R_* for KOI-94d; see Table 2). This supports the notion that these three planets are indeed revolving around the same host star.

2.1.3. TTV signals

Fixing a/R_* , R_p/R_* , b , u_1 , and u_2 at the values in Table 3, we refit the transit light curves of each planet to find the values of t_c given in Tables 8 to 10 in Appendix A, with the values of reduced χ^2 and 1σ upper/lower limits obtained from the posterior. The column labeled as $O-C$ tabulates the residuals of a linear fit to t_c versus transit number, in which linear ephemerides in Table 4 are extracted. The values of reduced χ^2 of the linear fits in this table indicate the significant deviations of the transit times from the linear ephemerides (i.e. TTVs) for all the three planets, as shown in Figure 5. Note that the TTV of KOI-94c shows the modulation with the period of $(1/P_c - 2/P_d)^{-1} \simeq 155$ days, which clearly comes from near 2:1 resonance of KOI-94c and KOI-94d as pointed out by Xie et al. (2013) (see also Appendix B).

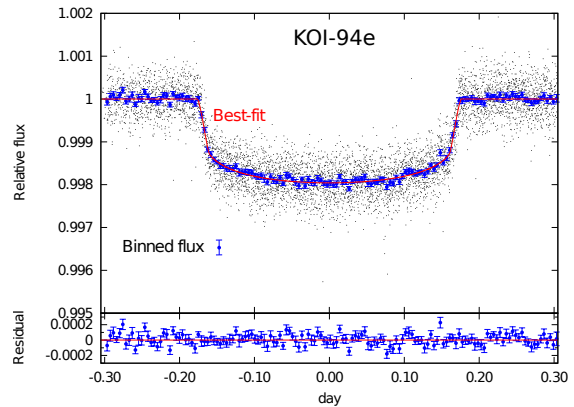


FIG. 4.— Phase-folded transit light curve of KOI-94e (same as Figure 2).

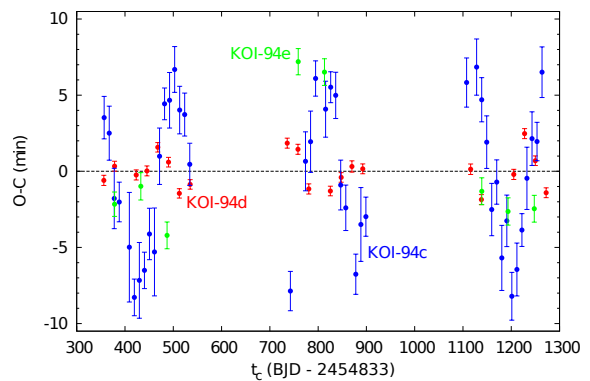


FIG. 5.— Observed TTV signals of KOI-94c (blue), KOI-94d (red), and KOI-94e (green).

2.2. Numerical analysis of the TTV signals using RV mass of KOI-94d

We numerically analyze the TTV signals in Figure 5 to constrain the masses, eccentricities, and longitudes of periastrons of KOI-94c, KOI-94d, and KOI-94e (nine parameters in total). In this section, we fix the mass of KOI-94d at $m_d = 106M_\oplus$, the best-fit RV value obtained by Weiss et al. (2013). Since this value is only marginally consistent with $m_d = 73 \pm 25M_\oplus$ obtained by Hirano et al. (2012) based on the out-of-transit RVs taken by the Subaru telescope, we also investigate the case of $m_d = 73M_\oplus$ here.

2.2.1. Calculation of the simulated TTV

Orbits of the planets are integrated using the fourth-order Hermite scheme with the shared time step (Kokubo & Makino 2004). The time step (typically ~ 0.025 days) is chosen so that the fractional energy change due to the integrator during ~ 1000 days integration should always be smaller than 10^{-9} . All the simulations presented in this section integrate planetary orbits beginning at the same epoch $T_0(\text{BJD}) = 2455189.1703$ (the first transit time of KOI-94d), until $\text{BJD} = 2456133.0$ (approximately the last transit time of KOI-94d we analyzed).

For each planet, the initial value of the orbital inclination i is fixed at the value obtained from a/R_* and b (see Table 3), assuming that $e = 0$. Here, all the i values are

TABLE 3
 REVISED TRANSIT PARAMETERS OBTAINED FROM PHASE-FOLDED LIGHT CURVES.

	KOI-94c	KOI-94d	KOI-94e
a/R_\star	$15.7798^{+0.0016}_{-0.0016}$	$26.24^{+0.20}_{-0.19}$	$47.4400^{+0.0094}_{-0.0093}$
R_p/R_\star	$0.025673^{+0.00074}_{-0.00075}$	$0.07029^{+0.00014}_{-0.00015}$	$0.04137^{+0.00012}_{-0.00013}$
b	$0.021^{+0.020}_{-0.015}$	$0.299^{+0.022}_{-0.025}$	$0.3840^{+0.0048}_{-0.0055}$
u_1	0.40 ± 0.06	0.40 ± 0.02	0.36 ± 0.07
u_2	$0.10^{+0.08}_{-0.09}$	0.14 ± 0.03	$0.19^{+0.11}_{-0.10}$
$\chi^2/\text{d.o.f}$	25843/23611	15473/13766	6822/5934

 NOTE. — The quoted error bars denote 1σ confidence intervals obtained from the posterior distributions. The values of a/R_\star and b for KOI-94c and KOI-94e are determined with the prior information about the stellar density based on the result for KOI-94d (see the main text).

 TABLE 4
 LINEAR EPHEMERIDES OF KOI-94c, KOI-94d, AND KOI-94e.

Parameter	KOI-94c	KOI-94d	KOI-94e
t_0 (BJD - 2454833)	138.00826 ± 0.00038	132.74103 ± 0.00012	161.23888 ± 0.00046
P (days)	10.4236888 ± 0.0000053	22.3429698 ± 0.0000036	54.319849 ± 0.000035
$\chi^2/\text{d.o.f}$	10.4	13.7	29.2

chosen in the range $[0, \pi/2]$.⁸ The values of Ω_d and Ω_e are fixed at those in Table 2. Since we have no information on the nodal angle of KOI-94c, we assume $\Omega_c = 0$ deg. Initial semi-major axes are calculated via Kepler’s third law with $M_\star = 1.25M_\odot$ (Hirano et al. 2012), orbital periods in Table 4, and planetary masses adopted in each simulation. The phases of the planets are determined from the transit ephemerides: for each planet, we convert the transit time closest to T_0 into the sum of the argument of periastron and mean anomaly $\omega + f$, taking account of the non-zero eccentricity if any, and then move it backward in time to T_0 , assuming a Keplerian orbit.

The mid-transit times of each planet are determined by minimizing the sky-plane distance D between the star and the planet, where the roots of the time derivative of D are found by the Newton-Raphson method (Fabrycky 2010). Then these transit times are fitted with a straight line and thereby the TTVs (= residuals of the linear fit), as well as the linear ephemeris (P and t_0), are extracted. We compute the chi squares of the simulated TTVs obtained in this way as

$$\chi_j^2 = \sum_{i:\text{observed transits}} \left[\frac{\text{TTV}_{\text{sim}}^{(j)}(i) - \text{TTV}_{\text{obs}}^{(j)}(i)}{\sigma_{\text{obs}}^{(j)}(i)} \right]^2, \quad (j = c, d, e) \quad (1)$$

where $\text{TTV}_{\text{sim}}^{(j)}(i)$ and $\text{TTV}_{\text{obs}}^{(j)}(i)$ are the i -th values of simulated and observed TTVs of planet j , respectively, and $\sigma_{\text{obs}}^{(j)}(i)$ is the observational uncertainty of the i -th transit time of planet j .

Note that we do not fit the transit times directly but only the *deviations* from the periodicity in our analysis, assuming that they provide sufficient information on the gravitational interaction among the planets. Indeed,

⁸ As we will see in Section 4, the observed PPE light curve requires that if we (arbitrarily) choose i_d in $[0, \pi/2]$, i_e is also in this range. There is no justification to choose i_c also in this range, but this choice does not affect the result significantly because the value of i_c is very close to $\pi/2$, as suggested by the small value of b_c (c.f. Table 3)

although the initial values of semi-major axes are chosen to match the observed periods, periods derived from the simulations are different typically by ~ 0.01 days. This is because strong gravitational interaction among massive, closely-packed planets in this system causes the oscillations of their semi-major axes with amplitudes dependent on the parameters of the planets adopted in each run. We will show that this simplified method still yields reasonable results in the last part of Section 2.4.

2.2.2. Estimates for the TTV amplitudes

Before directly fitting the observed TTV signals, we evaluate the contribution from each planet to the TTVs of KOI-94c, KOI-94d, and KOI-94e. We divide the four planets into six pairs and integrate circular orbits for each pair using the best-fit masses by Weiss et al. (2013) listed in Table 2. Semi-amplitudes of the resulting TTVs of KOI-94c, KOI-94d, and KOI-94e are shown in Table 5. Considering the uncertainties of transit times listed in Tables 8 to 10 (typically 1.4 min, 0.3 min, and 0.9 min for KOI-94c, KOI-94d, and KOI-94e, respectively), this result indicates that KOI-94b has negligible contribution for the TTVs of the other three. In the following analysis, therefore, we integrate the orbits of the other three planets (KOI-94c, KOI-94d, and KOI-94e) only. We also find that the TTVs of KOI-94c and KOI-94e are mainly determined by the perturbation from the neighboring planet KOI-94d, while that of KOI-94d depends on both of its neighbors. Such dependence is naturally understood from the architecture of this system (see Figure 1). Consequently, each planet’s TTV mainly depends on the parameters listed in the rightmost column of Table 5, where we define $\mathbf{e}_j = (e_j \cos \varpi_j, e_j \sin \varpi_j)$ ($j = c, d, e$). Note that the TTV of each planet is insensitive to its own mass. This is why m_j ($j = c, d, e$) is not included in the row for planet j .

2.2.3. Results

TTV of KOI-94e. — Since the TTV of KOI-94e is mainly determined by \mathbf{e}_d and \mathbf{e}_c (and m_d , of course, which we fix at the RV value), we fit it first so as to con-

TABLE 5
SEMI-AMPLITUDE OF THE SIMULATED TTV (IN UNITS OF MIN) FOR EACH PLANET PAIR.

TTV	pair				Major parameters for TTV
	KOI-94b	KOI-94c	KOI-94d	KOI-94e	
KOI-94c	$\lesssim 0.05$	-	11	$\lesssim 0.05$	m_d, e_c, e_d
KOI-94d	$\lesssim 0.05$	0.47	-	2.1	m_c, m_e, e_c, e_d, e_e
KOI-94e	$\lesssim 0.05$	0.15	0.83	-	$m_d, e_d, e_e, (m_c, e_c)$

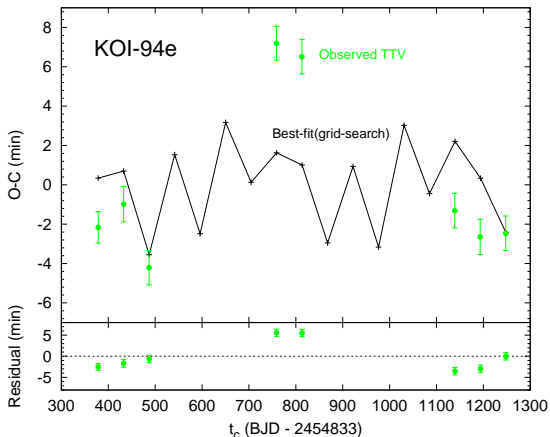


FIG. 6.— Best-fit simulated TTV of KOI-94e obtained by the grid-search for $m_d = 106M_\oplus$ (black crosses connected with the solid line) with observed data (green points). The best-fit corresponds to $e_d = (0.02, 0.02)$ and $e_e = (0.04, 0.02)$.

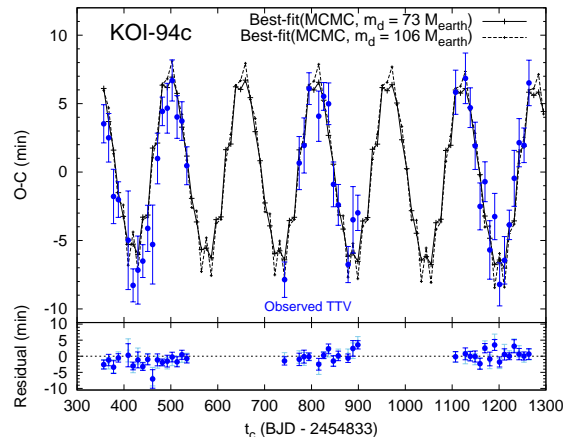


FIG. 7.— Best-fit simulated TTVs of KOI-94c obtained by the MCMC fit (black crosses connected with lines) with observed data (points with error bars). The result for $m_d = 73M_\oplus$ is plotted with solid lines (in $O-C$ plot) and blue points (in residual plot), and that for $m_d = 106M_\oplus$ with dashed lines and sky-blue points.

strain these parameters. We calculate χ_e^2 for $|e_d \cos \varpi_d|$, $|e_d \sin \varpi_d| \leq 0.06$ and $|e_e \cos \varpi_e|$, $|e_e \sin \varpi_e| \leq 0.25$ (which well cover the 1σ regions for these parameters obtained from the RVs) at the grid-spacing of 0.01, fixing $e_c = 0$ and planetary masses at the best-fit values from the RVs. However, we cannot fit the observed TTV well in both $m_d = 106M_\oplus$ and $73M_\oplus$ cases. The best-fit for the former case, which gives $\chi_e^2 = 122$ for 4 degrees of freedom, is shown in Figure 6. For this reason, in addition to the fact that we have only eight transits observed for KOI-94e, we decide not to use the TTV of this planet to constrain the system parameters, but fit only the TTVs of KOI-94c and KOI-94d. The large discrepancy in the amplitudes of simulated and observed TTVs may suggest another source of perturbation which is not included in our model, such as a non-transiting planet or other minor bodies.

Grid-search for an initial parameter set. — Then we perform the grid-search fit to the TTVs of KOI-94c and KOI-94d to find an appropriate initial parameter set for the following MCMC analysis. Based on the estimates given in Table 5, we fit these TTVs separately as follows. We first fit the TTV of KOI-94c varying e_c and e_d in $|e_j \cos \varpi_j|$, $|e_j \sin \varpi_j| \leq 0.10$ ($j = c, d$) at the grid-spacing of 0.01, and find one minimum of χ_c^2 for both $m_d = 106M_\oplus$ and $m_d = 73M_\oplus$ cases. Next, for all the sets of $(e_c, \varpi_c, e_d, \varpi_d)$ in 2σ ($m_d = 106M_\oplus$ case) or 1σ ($m_d = 73M_\oplus$ case) confidence regions around the minimum, we run integrations varying $e_e \cos \varpi_e$ and $e_e \sin \varpi_e$ from -0.1 to 0.1 at the grid spacing of 0.01, m_c from 0 to $24M_\oplus$ at the grid spacing of $6M_\oplus$, and m_e from 7 to $57M_\oplus$ at the grid spacing of $10M_\oplus$ (all of these cover the 1σ intervals from RV), to find the set of eight parameters

that best fits the TTV of KOI-94d.

MCMC fit to the TTVs of KOI-94c and KOI-94d. — Choosing the above set as initial parameters, we then simultaneously fit the TTVs of KOI-94c and KOI-94d using an MCMC algorithm. In this fit, we use $\chi_c^2 + \chi_d^2$ as the χ^2 statistic. The resulting best-fit parameters and their 1σ uncertainties are summarized in Table 6 for the two choices of m_d (the second and third columns). The best-fit simulated TTVs are plotted in Figures 7 and 8 for KOI-94c and KOI-94d, respectively.

Note that uncertainties of $e_c \cos \varpi_c$, $e_d \cos \varpi_d$, and $e_e \cos \varpi_e$ are relatively large for $m_d = 73M_\oplus$ case. This is because the posterior distributions of these parameters have two peaks, the smaller of which lies close to the best-fit value for $m_d = 106M_\oplus$ case. Considering this fact, the two results are roughly consistent with each other. Nevertheless, a total χ^2 in $m_d = 73M_\oplus$ case is smaller by 40 for 57 d.o.f. than in $m_d = 106M_\oplus$ case. This suggests that the TTV alone favors m_d smaller than the RV best-fit value, as will be confirmed in the next subsection.

2.3. Solution based only on TTV

In order to obtain a solution independent of RVs, we perform the same MCMC analysis of TTVs of KOI-94c and KOI-94d, this time also allowing m_d to float. Since the above analyses suggest that the eccentricities of all the planets are small, we choose circular orbits with the best-fit RV masses as an initial parameter set. The resulting best-fit parameters are summarized in Table 6, and the corresponding best-fit simulated TTVs are shown in Figures 9 and 10. As expected, we find a solution with small eccentricities and with m_d smaller than

TABLE 6
 BEST-FIT PARAMETERS OBTAINED FROM TTV ANALYSIS.

Parameter	Value ($m_d = 106M_\oplus$)	Value ($m_d = 73M_\oplus$)	Value (TTV only)
KOI-94c			
m_c (M_\oplus)	$11.8^{+1.6}_{-1.5}$	$13.9^{+2.7}_{-2.7}$	$9.4^{+2.4}_{-2.1}$
$e_c \cos \varpi_c$	$0.0329^{+0.0047}_{-0.0055}$	$0.0092^{+0.0264}_{-0.0050}$	$0.0143^{+0.0080}_{-0.0059}$
$e_c \sin \varpi_c$	$-0.0104^{+0.0038}_{-0.0042}$	$-0.0031^{+0.0067}_{-0.0061}$	$0.0045^{+0.0091}_{-0.0079}$
χ_c^2	84	62	56
KOI-94d			
m_d (M_\oplus)	106 (fixed)	73 (fixed)	$52.1^{+6.9}_{-7.1}$
$e_d \cos \varpi_d$	$0.055^{+0.011}_{-0.014}$	$-0.016^{+0.064}_{-0.011}$	$-0.022^{+0.014}_{-0.011}$
$e_d \sin \varpi_d$	$0.012^{+0.011}_{-0.012}$	$0.009^{+0.018}_{-0.018}$	$0.008^{+0.021}_{-0.018}$
χ_d^2	66	48	43
KOI-94e			
m_e (M_\oplus)	$15.9^{+2.4}_{-2.2}$	$12.9^{+3.0}_{-2.3}$	$13.0^{+2.5}_{-2.1}$
$e_e \cos \varpi_e$	$0.067^{+0.014}_{-0.019}$	$-0.069^{+0.120}_{-0.018}$	$-0.078^{+0.021}_{-0.014}$
$e_e \sin \varpi_e$	$0.042^{+0.012}_{-0.017}$	$-0.022^{+0.032}_{-0.016}$	$-0.025^{+0.017}_{-0.014}$
$(\chi_c^2 + \chi_d^2)/\text{d.o.f}$	150/57	110/57	99/56

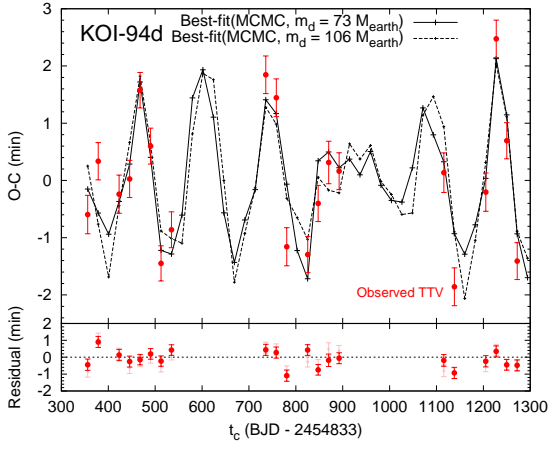


FIG. 8.— Best-fit simulated TTVs of KOI-94d obtained by the MCMC fit (black crosses connected with lines) with observed data (points with error bars). The result for $m_d = 73M_\oplus$ is plotted with solid lines (in $O - C$ plot) and red points (in residual plot), and that for $m_d = 106M_\oplus$ with dashed lines and pink points.

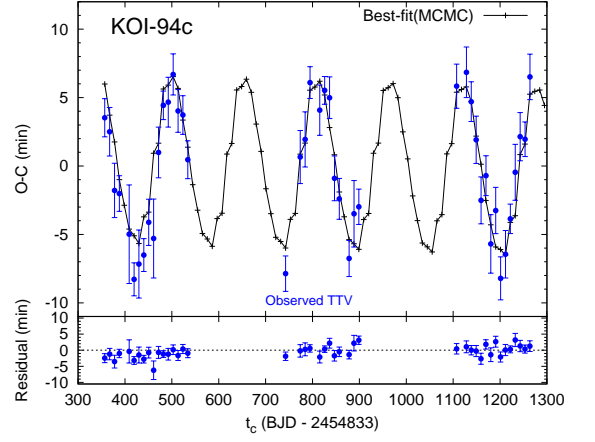


FIG. 9.— Best-fit simulated TTV of KOI-94c based on the TTV data alone (black crosses connected with lines) with observed data (blue points).

the RV best-fit value. This solution is similar to that for $m_d = 73M_\oplus$ case, except that m_d is even smaller.

2.4. Discussion: comparison with the RV results

While the values of e_d and e_e obtained in our TTV analysis are consistent with the RV values in Table 2, the best-fit e_c obtained from the TTV is $\sim 1.8\sigma$ smaller than the RV best-fit ($e_c = 0.43 \pm 0.23$). Considering the marginal detection of KOI-94c's RV and the dynamical stability of the system, however, the TTV value seems to be preferred. In fact, this value is robustly constrained by the clear TTV signal of KOI-94c; in the grid-search performed in Section 2.2.3, we searched the region where $e_c \lesssim 0.14$ to fit the TTV of this planet, but the resulting χ_c^2 strongly disfavored large e_c regions in both $m_d = 106M_\oplus$ and $m_d = 73M_\oplus$ cases.

The TTV values of m_c and m_e are consistent with the RV results, but m_e is constrained to a rather lower value than the RV best-fit. Using this value, along with the photometric values of R_p/R_\star and ρ_\star , and spectroscopic value of M_\star , the density of KOI-94e is given by $\rho_e \sim$

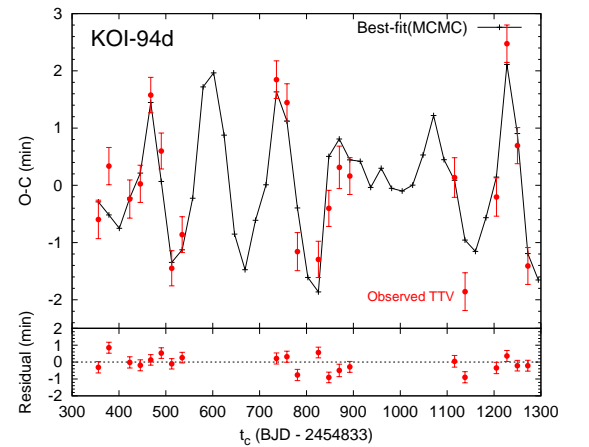


FIG. 10.— Best-fit simulated TTV of KOI-94d based on the TTV data alone (black crosses connected with lines) with observed data (red points).

0.3 g cm^{-3} . This implies that it is one of the lowest-density planets ever discovered.

The largest discrepancy arises in the value of m_d , mass of KOI-94d, for which the TTV best-fit value is smaller than the RV value by $\sim 4\sigma$. The worse fit in the case of $m_d = 106M_\oplus$ is mainly due to the fact that the observed TTV amplitude of KOI-94c is smaller than expected from this value of m_d . As shown in Table 5, the TTV of this planet is completely dominated by the perturbation from KOI-94d, and so the parameters relevant to this TTV are m_d , e_c , and e_d . Table 5 also shows that $m_d = 106M_\oplus$ leads to the TTV semi-amplitude of ~ 11 min for $e_c = e_d = 0$, which is much larger than the observed TTV amplitude of KOI-94c (see Figure 5). As a result, the values of e_c and e_d are fine-tuned to fit the observed signal, resulting in strict constraints on these parameters. The problem is that these values of e_c and e_d do not fit the TTV of KOI-94d well. In the grid-search, we first fit the TTV of KOI-94c alone, and the best-fit gives $\chi_c^2 = 66$ for $m_d = 106M_\oplus$. However, this value is largely increased in the simultaneous MCMC fit to the TTVs of KOI-94c and KOI-94d (Table 6), which means that these two TTVs cannot be explained with the same set of e_c and e_d . On the other hand, this tension does not exist in $m_d = 73M_\oplus$ case, in which both of the grid-search and MCMC return the same values for the best-fit χ_c^2 . In fact, the analysis using the analytic formulae of TTVs from two coplanar planets lying near $j : j - 1$ resonance (Lithwick et al. 2012) also supports the above reasoning, suggesting that m_d expected from the TTV of KOI-94c is rather small (see Appendix B).

For these reasons, it is clear that the TTV favors the solution with m_d smaller than the RV best-fit value. It is also true, however, that the RV of KOI-94d is detected with high significance, in contrast to those of the other planets. Indeed, we calculate the RVs using the best-fit TTV parameters and find that the resulting amplitude is much smaller than that observed by Weiss et al. (2013). Since its origin is not yet clear, this discrepancy motivates further investigation of KOI-94 including additional RV/TTV observations.

Finally, we note again that in the above analysis we just fit the *TTVs* rather than the *transit times* of KOI-94c and KOI-94d. For this reason, our solution corresponds to the planetary orbits whose periods are slightly different from the actually observed values. One may argue that such an approximate method leads to an incorrect solution. In order to assure that this is not the case, we fit the transit times of the two planets, choosing m , a , $e \cos \varpi$, $e \sin \varpi$, and $\omega + f$ of KOI-94c, KOI-94d, and KOI-94e at time T_0 as free parameters (fifteen parameters in total). We run two MCMC chains starting from (i) circular orbits with RV best-fit masses and (ii) a local minimum reached by the Levenberg-Marquardt method (Markwardt 2009) starting from the TTV best-fit parameters (rightmost column of Table 6). We find that the best-fit values of (m, e, ϖ) obtained in these ways show similar trends as the TTV best-fit in Section 2.3, giving comparable reduced χ^2 values. Namely, the mass of KOI-94d is much smaller than the RV best-fit and eccentricities of the three planets are close to zero.

Incidentally, as in the case of the fit to TTVs, the transit times of KOI-94d are less well reproduced than those of KOI-94c. In fact, the fit to transit times gives a bet-

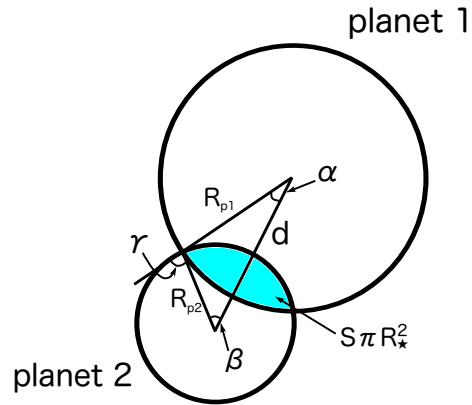


FIG. 11.— Two overlapping planets 1 and 2. The definitions of angles α , β , and γ are shown. Area of the shaded region corresponds to S in Eq.(2) times the area of the stellar disk.

ter χ_c^2 than that to TTVs because the small linear trend apparent in the lower panel of Figure 9 is removed; on the other hand, χ_d^2 values are not so different in both cases. The difficulty in completely reproducing the orbit of KOI-94d may also indicate the presence of the additional perturber discussed in Section 2.2.3.

3. ANALYTIC FORMULATION OF THE PPE

In this section, we present a general analytic model of the PPE caused by two planets 1 and 2 on circular orbits (see Appendix C for the formulation taking account of $O(e)$ terms). In what follows, we use the stellar radius R_\star as the unit length because all the observables are only related to the lengths normalized to this value.

3.1. Flux variation due to a PPE

A PPE is observed as an increase in the relative flux of a star (or a “bump” in the light curve) during the double transit of two planets. Assuming that the two overlapping planets are spherical and neglecting the effect of limb-darkening, the increase in the relative flux S is given by the area of overlapping region of the two planets divided by that of the stellar disk (Figure 11):

$$S = \begin{cases} 0 & \text{for } R_{p1} + R_{p2} < d, \\ \frac{1}{2\pi} R_{p1}^2 (2\alpha - \sin 2\alpha) + \frac{1}{2\pi} R_{p2}^2 (2\beta - \sin 2\beta) & \text{for } |R_{p1} - R_{p2}| < d < R_{p1} + R_{p2}, \\ (\min(R_{p1}, R_{p2}))^2 & \text{for } d < |R_{p1} - R_{p2}|, \end{cases} \quad (2)$$

where d is the distance between the centers of the two planets in the plane of the sky, and the angles α and β are defined as

$$\cos \alpha = \frac{R_{p1}^2 + d^2 - R_{p2}^2}{2R_{p1}d}, \quad \cos \beta = \frac{R_{p2}^2 + d^2 - R_{p1}^2}{2R_{p2}d}. \quad (3)$$

An alternative expression of S for $|R_{p1} - R_{p2}| < d < R_{p1} + R_{p2}$ can be obtained from the derivative of S with respect to d . Using $d\alpha/dd$ and $d\beta/dd$ obtained from Eq.(3) and $R_{p1} \sin \alpha = R_{p2} \sin \beta$, we obtain

$$\frac{dS}{dd} = -\frac{1}{\pi} \sqrt{-d^2 + 2(R_{p1}^2 + R_{p2}^2) - \left(\frac{R_{p1}^2 - R_{p2}^2}{d}\right)^2} \quad (4)$$

for $|R_{p1} - R_{p2}| < d < R_{p1} + R_{p2}$. Eq.(4) can be integrated from $R_{p1} + R_{p2}$ to d by changing the variable from d to

$$\gamma \equiv \alpha + \beta = \pi - \arccos\left(\frac{R_{p1}^2 + R_{p2}^2 - d^2}{2R_{p1}R_{p2}}\right). \quad (5)$$

The result is

$$S = \frac{1}{\pi} \left[\frac{R_{p1}^2 + R_{p2}^2}{2} \gamma - R_{p1}R_{p2} \sin \gamma - (R_{p1}^2 - R_{p2}^2) \arctan\left(\frac{R_{p1} - R_{p2}}{R_{p1} + R_{p2}} \tan \frac{\gamma}{2}\right) \right]. \quad (6)$$

Here, S is given as a function of a single angle γ . These two expressions of S show that the shape of a bump due to a PPE is solely determined by d as a function of time, which will be derived in the following subsection.

The effect of limb-darkening can be included in our model by multiplying S by a factor that corresponds to the limb-darkening at the position on the stellar disk over which a PPE occurs. We adopt the quadratic limb-darkening law

$$I(\mu)/I(0) = 1 - u_1(1 - \mu) - u_2(1 - \mu)^2, \quad (7)$$

where $\mu = (1 - r^2)^{1/2}$ and r is the radial coordinate on the stellar disk. For a PPE that occurs totally within the stellar disk, the approximation by Mandel & Agol (2002), which is valid for a small planet whose radius is less than about $0.1R_*$, yields the modified relative increase S' as

$$S' = S \cdot \frac{I(r_*)}{\int_0^1 dr 2r I(r)} = S \cdot \frac{1 - u_1(1 - \mu_*) - u_2(1 - \mu_*)^2}{1 - u_1/3 - u_2/6}, \quad (8)$$

where r_* is the distance to the overlapping region. During the whole PPE, r_* is given in terms of d , $\Delta R_{12}^2 \equiv R_{p1}^2 - R_{p2}^2$, and r_j ($j = 1, 2$), the radial coordinate of the planet j 's center, as $r_* = \sqrt{(r_1^2 + r_2^2)/2 - d^2/4 + (r_2^2 - r_1^2 + \Delta R_{12}^2/2)\Delta R_{12}^2/2d^2}$.

3.2. Distance between the planets during a double transit

Hereafter, we adopt the Cartesian coordinate system (X, Y, Z) centered on the star, where the $+Z$ -axis is chosen in the direction of our line of sight, and X - and Y -axes are in the plane of the sky, forming a right-handed triad. As stated in the note of Table 2, we align the $+X$ axis with the ascending node of a virtual circular orbit whose angular momentum vector is parallel to the stellar spin vector, without loss of generality. Using R for the three-dimensional distance between the planet and the star, the position of a planet is expressed as

$$X = R [\cos \Omega \cos(\omega + f) - \sin \Omega \sin(\omega + f) \cos i], \quad (9)$$

$$Y = R [\sin \Omega \cos(\omega + f) + \cos \Omega \sin(\omega + f) \cos i], \quad (10)$$

$$Z = R \sin(\omega + f) \sin i. \quad (11)$$

Suppose that the two planets 1 and 2 are on Keplerian orbits whose semi-major axes are a_1 and a_2 , respectively. Neglecting the corrections arising from the non-zero eccentricity, the two-dimensional position vectors \mathbf{r}_j ($j = 1, 2$) of these planets in the plane of the sky

can be written as

$$\mathbf{r}_j = \begin{pmatrix} a_j \cos \Omega_j \cos(\omega_j + f_j) - b_j \sin \Omega_j \sin(\omega_j + f_j) \\ a_j \sin \Omega_j \cos(\omega_j + f_j) + b_j \cos \Omega_j \sin(\omega_j + f_j) \end{pmatrix}. \quad (12)$$

If the transits of the two planets are observed, a_j , b_j , R_{pj} , and the periods P_j are obtained as in Section 2. In this case, the relative motion of the planets is completely described except for the dependence on the relative nodal angle defined as

$$\Omega_{21} = -\Omega_{12} = \Omega_2 - \Omega_1. \quad (13)$$

Note that photometric surveys determine the absolute value of b , but not its sign. For a single transiting planet, b is conventionally defined to be positive (or equivalently, i is chosen to be in the range $[0, \pi/2]$), because the choice of its sign does not affect the transit signals. For multiple transiting planets, however, a different choice of the relative signs of b corresponds to a different orbital configuration. In this paper, we choose b_1 to be positive (i.e. $0 \leq i_1 \leq \pi/2$), but allow b_2 to be either positive or negative (i.e. $0 \leq i_2 \leq \pi$). The sign of b_2 , as well as the relative nodal angle Ω_{21} , is determined from the observed data of a PPE event.

During a double transit by planets $j = 1$ and 2 , their phases at time t are given by

$$\omega_j + f_j = \frac{\pi}{2} + n_j(t - t_c^{(j)}), \quad (14)$$

where $n_j = 2\pi/P_j$ is the mean motion and $t_c^{(j)}$ is the central transit time of planet j in this double transit. We then expand Eq.(12) to the first order of $n(t - t_c) \sim \mathcal{O}(a^{-1})$ to obtain

$$\mathbf{r}_j = \mathbf{v}_j(t - t_c^{(j)}) + \mathbf{r}_0^{(j)}, \quad (15)$$

where

$$\mathbf{v}_j = -a_j n_j \begin{pmatrix} \cos \Omega_j \\ \sin \Omega_j \end{pmatrix}, \quad \mathbf{r}_0^{(j)} = -b_j \begin{pmatrix} \sin \Omega_j \\ -\cos \Omega_j \end{pmatrix}. \quad (16)$$

These give the distance between the two planets d as⁹

$$d^2 = |\mathbf{r}_2 - \mathbf{r}_1|^2 = v^2 \left(t + \frac{r_0 \cos \theta_0}{v} \right)^2 + r_0^2 \sin^2 \theta_0, \quad (17)$$

where $\mathbf{v} \equiv \mathbf{v}_2 - \mathbf{v}_1$, $\mathbf{r}_0 \equiv \mathbf{r}_0^{(2)} - \mathbf{v}_2 t_c^{(2)} - \mathbf{r}_0^{(1)} + \mathbf{v}_1 t_c^{(1)}$, $v \equiv |\mathbf{v}|$, $r_0 \equiv |\mathbf{r}_0|$, and θ_0 is the angle between \mathbf{v} and \mathbf{r}_0 . Thus, the minimum value of d in this double transit

$$d_{\min} \equiv r_0 \sin \theta_0, \quad (18)$$

is reached at the time

$$t = t_{\min} \equiv -\frac{r_0 \cos \theta_0}{v}. \quad (19)$$

If $d_{\min} < R_{p1} + R_{p2}$, a PPE occurs during this double transit for a duration of

$$\Delta t = \frac{2}{v} \sqrt{(R_{p1} + R_{p2})^2 - d_{\min}^2}. \quad (20)$$

⁹ Strictly speaking, this expression of d contains $\mathcal{O}((n(t - t_c))^2)$ terms, and so we should use the second-order expansion in Eq.(15). Nevertheless, this only introduces the correction of order $(b/a)^2 \sim a^{-2}$, which can be safely neglected in our treatment below.

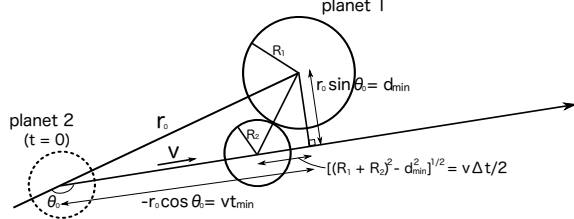


FIG. 12.— Geometry of the PPE. The relations between $(d_{\min}, t_{\min}, \Delta t)$ and (v, r_0, θ_0) are depicted. Note that the relative position of planet 2 at $t = 0$ is not its real position at the time, but is determined by extrapolating the linear orbit given by Eq.(15). This geometry shows that a PPE occurs only when $\cos \theta_0 < 0$, in which case t_{\min} given by Eq.(19) is always positive.

Eqs.(18) to (20) can be readily understood by considering the geometry of the PPE shown in Figure 12. The explicit expressions of v , r_0 , and $\cos \theta_0$ are

$$v^2 = a_1^2 n_1^2 + a_2^2 n_2^2 - 2a_1 n_1 a_2 n_2 \cos \Omega_{21}, \quad (21)$$

$$r_0^2 = (a_1 n_1 t_c^{(1)})^2 + (a_2 n_2 t_c^{(2)})^2 + b_1^2 + b_2^2 + 2(a_1 n_1 t_c^{(1)} b_2 - a_2 n_2 t_c^{(2)} b_1) \sin \Omega_{21} - 2(a_1 n_1 t_c^{(1)} a_2 n_2 t_c^{(2)} + b_1 b_2) \cos \Omega_{21}, \quad (22)$$

$$\cos \theta_0 = \frac{1}{v r_0} \left[-(a_1 n_1)^2 t_c^{(1)} - (a_2 n_2)^2 t_c^{(2)} + (a_2 n_2 b_1 - a_1 n_1 b_2) \sin \Omega_{21} + a_1 n_1 a_2 n_2 (t_c^{(1)} + t_c^{(2)}) \cos \Omega_{21} \right]. \quad (23)$$

3.3. Reconstruction of the mutual inclination Ω_{21}

The observed shape of a bump is characterized by its maximum height S_{\max} , central time t_{\min} , and duration Δt . If the bump is not saturated, i.e. $d_{\min} > |R_{p1} - R_{p2}|$, S_{\max} is uniquely translated into d_{\min} via Eq.(2). In this case, we can use Eqs.(18) to (20), the expressions for the three observables of a bump (d_{\min} , t_{\min} , Δt), to calculate

$$v = \frac{2}{\Delta t} \sqrt{(R_{p1} + R_{p2})^2 - d_{\min}^2}, \quad (24)$$

$$r_0^2 = d_{\min}^2 + (v t_{\min})^2 = d_{\min}^2 + \left(\frac{2 t_{\min}}{\Delta t} \right)^2 [(R_{p1} + R_{p2})^2 - d_{\min}^2], \quad (25)$$

$$\tan \theta_0 = -\frac{d_{\min}}{v t_{\min}} = -\frac{\Delta t}{2 t_{\min}} \frac{d_{\min}}{\sqrt{(R_{p1} + R_{p2})^2 - d_{\min}^2}}. \quad (26)$$

Furthermore, Eqs.(21) and (22), the explicit expressions for v and r_0 , are rewritten as

$$\cos \Omega_{21} = \frac{a_1^2 n_1^2 + a_2^2 n_2^2 - v^2}{2 a_1 a_2 n_1 n_2}, \quad (27)$$

$$\sin \Omega_{21} = \frac{r_0^2 - x_1^2 - x_2^2 + 2(\mathbf{x}_1 \cdot \mathbf{x}_2) \cos \Omega_{21}}{2 |\mathbf{x}_1 \times \mathbf{x}_2|}, \quad (28)$$

where we define $\mathbf{x}_1 = (a_1 n_1 t_c^{(1)}, b_1)$ and $\mathbf{x}_2 = (a_2 n_2 t_c^{(2)}, b_2)$. In this way, the relative nodal angle Ω_{21} can be specified explicitly from $(d_{\min}, t_{\min}, \Delta t)$ along with the photometrically obtained parameters

$(a_j, b_j, n_j, t_c^{(j)}, R_{pj})$, provided that the sign of b_2 is determined. Although we do not present any general procedure to determine the sign of b here, it is possible to do so at least empirically, as described in Section 4. Eq.(28) shows that $\sin \Omega_{21}$ is only weakly constrained when $a_1 n_1 / b_1 \simeq a_2 n_2 / b_2$, in which case the coefficients in front of $\sin \Omega_{21}$ in Eqs.(22) and (23) are close to zero because $t_c^{(1)} \simeq t_c^{(2)}$.

In the case of $d_{\min} < |R_{p1} - R_{p2}|$, only the upper limit on d_{\min} can be obtained, and so the entire shape of the bump is required to determine Ω_{21} .

Note that the formulation in this section is also valid even in the presence of non-Keplerian effects. In such a case, the Keplerian orbital elements in this formulation should be interpreted as the osculating orbital elements around a certain double transit.

4. APPLICATION TO THE PPE OBSERVED IN THE KOI-94 SYSTEM

Hirano et al. (2012) fit the whole light curve of the PPE for u_1 , u_2 , $t_c^{(1)}$, $t_c^{(3)}$, and Ω_{de} using an MCMC algorithm, and estimated the relative nodal angle between KOI-94d (planet 1 in Section 3) and KOI-94e (planet 2 in Section 3) to be $\Omega_{\text{ed}} = 1.15 \pm 0.55$ deg.¹⁰ In their analysis, the light curve is modeled as a sum of two single transit light curves (Ohta et al. 2009) and the bump function, which is calculated essentially in the same way as described in Section 3, but neglecting the effect of limb-darkening. In this section, we confirm that this is a unique solution expected from the observed features of the bump, based on analytic expressions obtained in the previous section.

The top panel of Figure 13 plots d_{\min} as a function of Ω_{ed} in the double transit during which the PPE was observed, calculated by Eqs.(18), (22), and (23). In Figure 13, we fix a_j , b_j , n_j , and R_{pj} at the values publicized by the Kepler team (Table 2), and $t_c^{(j)}$ at the best-fit values obtained by Hirano et al. (2012). The red and blue lines correspond to the cases of $b_e > 0$ and $b_e < 0$, respectively, and the solid parts of the lines show the range of Ω_{ed} for which the PPE occurs, i.e., $d_{\min} < R_{pd} + R_{pe}$. This panel implies that the PPE itself could have occurred for a wide range of Ω_{ed} except for those around ± 50 deg. The central time t_{\min} and duration Δt for a specific value of Ω_{ed} can be obtained from the middle and bottom panels. These also indicate that a wide variety of bumps could have resulted.

Indeed, these three observables have enough information to reconstruct the value of Ω_{ed} , in addition to the sign of b_e . As for the observed eclipse, the best-fit light curve yields $S_{\max} \approx 3.88 \times 10^{-4}$, $t_{\min} \approx 378.508$ day (BJD - 2454833), and $\Delta t \approx 0.076$ days. Eq.(2) shows that the above value of S_{\max} uniquely translates into $d_{\min} \approx 0.0829$. The values of these d_{\min} , t_{\min} , and Δt are plotted in Figure 13 in horizontal dashed lines.¹¹ For the observed value of d_{\min} , Figure 13 allows eight solutions, four for each of $b_e > 0$ and $b_e < 0$. However, the asymmetry of t_{\min} curve in the middle panel of Figure

¹⁰ Note that the ‘‘mutual inclination’’ δ defined in Hirano et al. (2012) corresponds to $\Omega_{\text{de}} = -\Omega_{\text{ed}}$ in our definition.

¹¹ The analysis that includes the effect of limb-darkening by Eq.(8) returned the same values of d_{\min} , t_{\min} , and Δt with a slightly different $\Omega_{\text{ed}} \sim 1.21$ deg, in which case the following discussion is also valid.

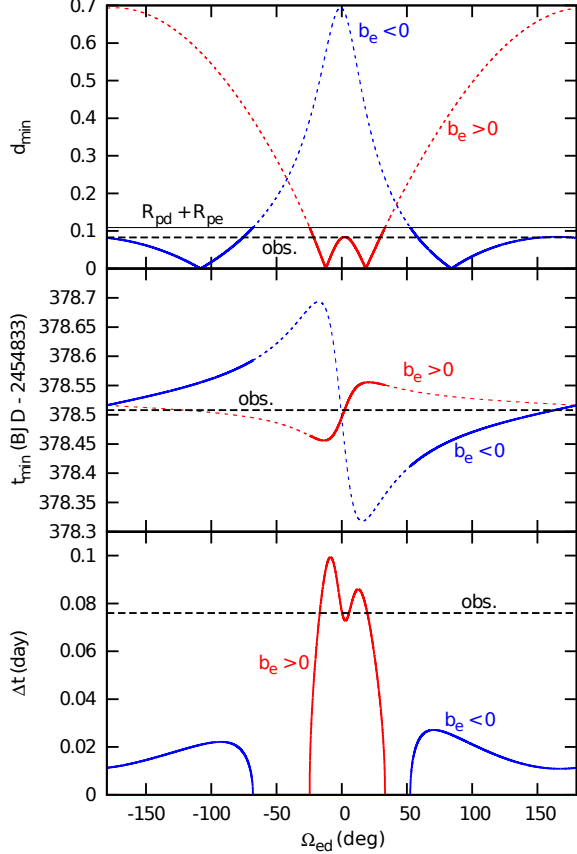


FIG. 13.— Plots to determine Ω_{ed} and the sign of b_e from the observed bump features. (Top) Relation between d_{\min} and Ω_{ed} based on Eqs.(18), (22), and (23). The red and blue lines correspond to $b_e > 0$ and $b_e < 0$, respectively. The solid parts show the region where d_{\min} is less than $R_{pd} + R_{pe}$ (black solid line), i.e., the PPE occurs. The dashed black line shows the value of d_{\min} obtained from the best-fit for the observed PPE light curve. (Middle) Relation between t_{\min} and Ω_{ed} based on Eqs.(19) and (21) to (23). (Bottom) Relation between Δt and Ω_{ed} based on Eqs.(20), (18), and (21) to (23).

13 shows that only the solutions around $\Omega_{ed} \sim 0$ deg (slightly positive, $b_e > 0$) or $\Omega_{ed} \sim 180$ deg ($b_e < 0$) are possible. These correspond to the nearly parallel and anti-parallel planetary orbits, respectively. This degeneracy can be broken with the value of Δt : the retrograde (anti-parallel) orbit results in a much shorter bump due to the larger relative velocity between the planets than the prograde (parallel) case. The bottom panel of Figure 13 shows that the observed duration allows only the prograde orbit with $b_e > 0$. In this way, $\Omega_{ed} = 1.15$ deg (and $b_e > 0$) proves to be the unique solution that reproduces the observed features of the bump. In fact, one can show that any set of $(d_{\min}, t_{\min}, \Delta t)$ allows the unique determination of Ω_{ed} in the case discussed here. Mathematically, this comes from the fact that the curve $(d_{\min}, t_{\min}, \Delta t)$ parametrized by Ω_{ed} has no self-intersection.

Combining Ω_{ed} with the result of the spin-orbit angle measurement, both Ω_d and Ω_e can be constrained. Since we have assumed that $b_d > 0$ or $0 \leq i_d \leq \pi/2$, the observed spin-orbit angle λ is equal to Ω_d in our definition, and so $\Omega_d = -6_{-11}^{+13}$ deg. Thus, $\Omega_{ed} = \Omega_e - \Omega_d = 1.15 \pm 0.55$ deg (Hirano et al. 2012) gives $\Omega_e = -5_{-11}^{+13}$ deg

(Table 2). Using these two parameters along with the transit parameters in Table 2, we trace the orbits of KOI-94d and KOI-94e for one hundred years, assuming that their orbits never change over time. The result of this calculation indicates that the next PPE will occur in the double transit around BJD = 2461132.4 (date in UT 2026 April 1/2), which is the third double transit after the one discussed here. The same conclusion is obtained even when we vary Ω_{ed} within its 3σ interval. In a real system, however, it is not at all obvious that the next PPE will occur in this double transit, because orbital elements do change over time; in the next section, we discuss how the mutual gravitational interaction among the planets affects this result.

5. IMPLICATION FOR THE NEXT PPE: THE EFFECT OF MULTI-BODY INTERACTION

In Section 2, we obtained a set of system parameters by analyzing photometric light curves of the three planets. Based on this result, we now address the question whether the PPE will occur in the same double transit as predicted in Section 4, even in the presence of the mutual gravitational interaction among the planets.

5.1. Fixing double-transit parameters

In order to determine the relative nodal angle crucial in predicting the next PPE, we refit the transit light curve around BJD = 2454211.5, in which the PPE was observed. We model the light curve as described in Section 4 including the effect of limb-darkening to obtain R_{pd} , R_{pe} , a_d , a_e , b_d , b_e , $t_c^{(d)}$, $t_c^{(e)}$, and Ω_{ed} . Here, the same prior as used in fitting the phase-folded light curve is assumed to fix the value of a_e . We adopt the limb-darkening coefficients obtained from the light curve of KOI-94d, $u_1 = 0.40$ and $u_2 = 0.14$, which are determined with the best precision among the three planets. The result is summarized in Table 7.

In this fit, R_{pd}/R_* is different from our revised mean value ($R_{pd}/R_* = 0.07029_{-0.00015}^{+0.00014}$) by 1.7σ . We suspect that this difference comes from the systematics introduced in the detrending procedure. When an artifact or some other astrophysical processes (e.g. star spots) accidentally increase the relative flux just before (or after) the transit, the result of detrending is biased towards such features in setting the baseline of the transit light curve. If we use a wider range of data points, the effect of such a small feature is averaged out and does not change the result so significantly. In contrast, if a narrow region around a transit is used, the baseline is somewhat distorted and the resulting detrended light curve becomes either deeper or shallower. Such systematics are averaged in the phase-folded light curves, but may be significant in an individual transit. In the case of the double transit light curve analyzed here, the relative flux begins to increase just before the ingress, and the depth of the transit is shallower in the first half of the transit than in the latter, making the light curve slightly asymmetric. This feature, along with the fact that the revised R_{pd} gives better χ^2 in all the other transit light curves than R_{pd} given by the Kepler team, suggests that the discrepancy in R_{pd} is caused by such an incidental brightening. To test this scenario, we repeat the analysis above changing the span of detrending from ~ 1 day to ~ 0.5 days,

TABLE 7
BEST-FIT PARAMETERS FOR THE PPE LIGHT CURVE.

Parameter	Best-fit value
R_{pd}/R_\star	0.06954 ± 0.00043
R_{pe}/R_\star	0.04123 ± 0.00070
a_d/R_\star	26.21 ± 0.082
a_e/R_\star	47.44 ± 0.027
b_d	0.2951 ± 0.0092
b_e	0.3693 ± 0.0095
$t_c^{(d)}$ (BJD - 2454833)	378.51372 ± 0.00023
$t_c^{(e)}$ (BJD - 2454833)	378.51785 ± 0.00060
Ω_{ed} (deg)	1.13 ± 0.52
$\chi^2/\text{d.o.f}$	746/687

and find that the resulting mean transit parameters are consistent with those above, but the depth of the double-transit light curve becomes deeper, consistently with our revised parameters.

5.2. Evaluation of the multi-body effect

The occurrence of the PPE in the multi-body context can be assessed in a similar way as in Section 4; we compare $R_{pd} + R_{pe}$ with d_{\min} calculated from Eqs.(18), (22), and (23), but this time the variation of orbital elements must be taken into account. Specifically, we need to evaluate the variations of the parameters relevant to d_{\min} , i.e., scaled semi-major axis a/R_\star , mean motion n , transit center of the double transit t_c , impact parameter b , and nodal angle Ω (as long as the eccentricities are small). In order to give an estimate for these variations, we integrate the orbits of the three planets using the best-fit (m, e, ϖ) in the rightmost column of Table 6 up to BJD = 2461132.4, the double transit in which the PPE is expected from the two-body analysis in Section 4. The results are the following:

1. The oscillation amplitudes of a_d and a_e are less than 5×10^{-5} AU ($\sim 0.03\%$) and 4×10^{-4} AU ($\sim 0.13\%$), respectively. Since these are much smaller than the observed uncertainties of a_d/R_\star and a_e/R_\star ($\sim 1\%$), the multi-body effect can be neglected for these two parameters.
2. Corresponding to the oscillations in semi-major axes above, n_d and n_e also show the modulations whose peak-to-peak amplitudes are $\sim 2\pi(0.01 \text{ day})^{-1}$ and $\sim 2\pi(0.1 \text{ day})^{-1}$, respectively. These are much larger than the uncertainties in n_d and n_e that come from those in P_d and P_e , and so the multi-body effect is important for these parameters.
3. The differences of the periods calculated from the transit centers in the first ~ 1000 days (the range in which we analyzed the TTVs) of integration and from the whole orbit are at most comparable to the observed uncertainties of these parameters in Table 4. Thus the uncertainties of $t_c^{(d)}$ and $t_c^{(e)}$ can be evaluated using those of P and t_0 in the table. Note that the effect of TTV is taken into account in obtaining these errors.
4. Monotonic increase in i_d and decrease in i_e lead to at most $\sim 30\%$ variations of b_d and b_e , larger

than the observed errors. The multi-body effect is dominant for these parameters.

5. Ω_d/Ω_e also monotonically increases/decreases, but only by < 0.03 deg. This means that the uncertainty in the relative nodal angle Ω_{ed} is completely dominated by the error in Table 7, and the multi-body effect is negligible.

The above results indicate that the multi-body effect is the most significant for b_d and b_e . In order to relate the values of these parameters to the occurrence of the PPE during the double transit around BJD = 2461132.4, we use Eq.(18), (22), and (23) to calculate the maximum value of d_{\min} during this double transit in terms of b_d and b_e , varying (i) a_d , a_e , $t_c^{(d)}$, $t_c^{(e)}$, and Ω_{ed} within 1σ intervals calculated from the photometric errors, and (ii) n_d and n_e by the amplitudes of modulations estimated above. The region of (b_d, b_e) plane in which $d_{\min} < R_{pd} + R_{pe}$, i.e., the PPE occurs in this double transit, is shown in Figure 14 with light-gray shade.¹² When we vary the parameters in the set (i) within their 2σ and 3σ intervals, the edges of the shaded region can be as narrow as black solid and dashed lines. In fact, the gray-shaded region is mainly determined by the difference between b_d and b_e , as seen from this figure, and the edge of this region is found to be most sensitive to the uncertainties in $t_c^{(d)}$ and $t_c^{(e)}$. The former fact originates from the well-aligned orbital planes of KOI-94d and KOI-94e: since their orbital planes are nearly parallel in the plane of the sky, the minimum separation during the double transit in which KOI-94d overtakes KOI-94e is nearly the same as the difference between b_d and b_e . However, if their transit times are too far away from each other, such closest encounter may occur out of the double transit. This explains the latter feature. The PPE occurrence for different choices of (m, e, ϖ) can be judged by evaluating the variation of b_d and b_e in this plot. Since the variations of a , n , t_c , and Ω_{ed} would be of the same order as long as the resulting TTVs are consistent with the observation, we fix the shaded area in Figure 14 determined by these parameters. We perform a similar MCMC calculation as in Section 2.3 to obtain the distribution of (b_d, b_e) in the double transit at issue; we fit the observed TTVs again using the same χ^2 , but this time extend the orbit integration up to BJD = 2461132.4 and record the

¹² Here, the small uncertainties in R_{pd} and R_{pe} are neglected.

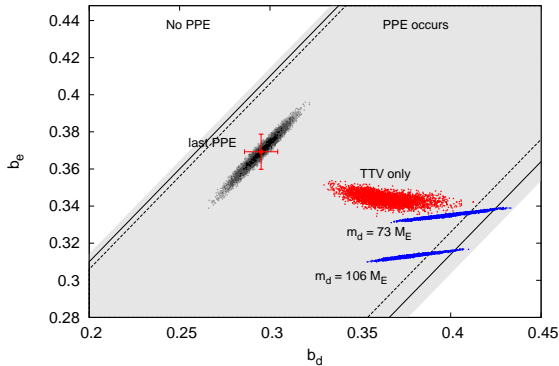


FIG. 14.— Relation between the occurrence of the PPE by KOI-94d and KOI-94e and the values of their impact parameters in the double transit around BJD = 2461132.4. If (b_d, b_e) in this double transit is inside the gray-shaded region, PPE occurs for all the values of photometrically derived parameters within 1σ of their best-fit values. When we vary them within their 2σ and 3σ intervals, the corresponding boundaries become black solid and dashed lines, respectively. The values of (b_d, b_e) at the last PPE is shown by the red point with error bars, and black, dark-gray, and light-gray points around it respectively show their 1σ , 2σ , and 3σ confidence regions. Red and blue points are the distributions of (b_d, b_e) in the double transit around BJD = 2461132.4 for the three different solutions in Table 6. The scattering of each set of points reflects the uncertainties in (m, e, ϖ) .

final values of b_d and b_e calculated via $b = a \cos i / R_*$.¹³ The resulting distribution of (b_d, b_e) is plotted with red points in Figure 14. We also repeat the same procedures fixing $m_d = 106M_\oplus$ and $m_d = 73M_\oplus$, and the distributions for these cases are plotted with blue points for comparison. In these calculations, we choose the initial values of i_d and i_e based on $(b_d, b_e) = (0.2951, 0.3693)$ in Table 7, a red point with error bars in Figure 14, rather than the mean values obtained from the phase-folded light curves in Table 3. This is because the mean parameters do not take account of the actual occurrence of the PPE. The black, dark-gray, and light-gray points around the double-transit value in Figure 14 respectively show its 1σ , 2σ , and 3σ confidence regions based on the posterior distribution of the double-transit fit. Here, the difference between b_d and b_e is rather sharply constrained by the minimum separation between the planets, namely, the height of the bump caused by the PPE. Even considering this uncertainty in the initial (b_d, b_e) , as well as the significant variation of impact parameters (or inclinations) due to the multi-body effect, (b_d, b_e) around BJD = 2461132.4 are well inside the region where the PPE occurs, at least within 1σ of transit and TTV parameters for all the three solutions.

For the best-fit (m, e, ϖ) obtained from the TTV alone, the expected height of the bump is much larger than in the last PPE (Figure 15), and so the detection of this PPE is highly feasible. In contrast, for (m, e, ϖ) based on the RV values of m_d , the bump height is com-

¹³ Here we adopt $R_* = (1.37 \pm 0.02)R_\odot$ obtained from photometric a_d/R_* , P_d , and spectroscopic M_* . This value is slightly smaller than $R_* = (1.52 \pm 0.14)R_\odot$ obtained by Weiss et al. (2013) using the Spectroscopy Made Easy (Valenti & Piskunov 1996), but this difference is consistent with the conclusion of Torres et al. (2012) that the $\log g$ value based on the Spectroscopy Made Easy is systematically underestimated for stars with $T_{\text{eff}} \gtrsim 6,000$ K.

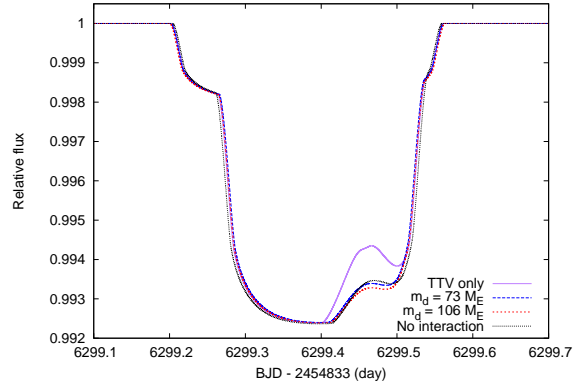


FIG. 15.— The expected light curves of the PPE in the double transit around BJD = 2461132.4 (date in UT 2026 April 1/2). The black dotted curve (No interaction) shows the result for the parameters in Table 7. The other curves use the median values of (b_d, b_e) for the three distributions in Figure 14, with other parameters fixed at the same values as above.

parable to the last PPE. This difference may be used to settle the difference of m_d values in RV and TTV analyses. For the RV-based solutions, the blue distributions in Figure 14 indicate that the PPE may not even happen when the variation of b_d is too large (corresponding to the large m_c values), and/or $\gtrsim 2\sigma$ deviations of $t_c^{(d)}$ and $t_c^{(e)}$ from the linear ephemerides make the shaded region too narrow for the PPE to occur (see solid and dashed lines).

We also check the other two double transits before the one discussed above (around BJD = 2457982 and BJD = 24583612), in case that the variations of b_d and b_e lead to the PPE which never happens without the interaction among the planets. In both of them, we find that the PPE does not happen for any possible values of b_d and b_e (from 0 to 1). Therefore, we can safely conclude that the next PPE will still occur during the same double transit as predicted by the two-body calculation, even when we include the mutual gravitational interaction among the planets.

6. SUMMARY AND DISCUSSION

We have performed an intensive TTV (transit timing variation) analysis in KOI-94, the first multi-planetary system exhibiting the PPE (planet-planet eclipse, Hirano et al. 2012). Comparison of the resulting system parameters with those estimated independently from the RV (radial velocity) data (Weiss et al. 2013) works as a valuable test to examine the reliability and limitation of the TTV analysis for other planetary systems for which the RV data are difficult to obtain. Furthermore, a possible discrepancy between the two estimates, if any, would be even useful in exploring additional planets or other interesting implications (e.g. Nesvorný et al. 2012).

Among the four planets reported so far, we considered the TTVs of KOI-94c, KOI-94d, and KOI-94e; we made sure that the contribution from the innermost and smallest planet KOI-94b is negligible at the current level of observational uncertainties.

We numerically integrated the orbits of the three planets that are directly incorporated in the MCMC search for the best-fit values of their masses, eccentricities,

and longitudes of periastrons; our best-fit values include $m_c = 9.4_{-2.1}^{+2.4} M_\oplus$, $m_d = 52.1_{-7.1}^{+6.9} M_\oplus$, $m_e = 13.0_{-2.1}^{+2.5} M_\oplus$, and $e \lesssim 0.1$ for all the three planets. Those results are in reasonable agreement with the RV results (Weiss et al. 2013), but we would like to note here a few possible interesting points.

1. Although the RV analysis results in a fairly large eccentricity for KOI-94c ($e_c = 0.43 \pm 0.23$), the TTVs indicate a significantly smaller value. In fact, the stability analysis of the system favors the TTV result.
2. The TTV best-fit value of m_d differs from the RV result $m_d = 106 \pm 11 M_\oplus$ by $\sim 4\sigma$ level. If the TTV value is correct, KOI-94d may be inflated, in contrast to the conclusion obtained by Weiss et al. (2013).
3. The TTV of the outermost planet KOI-94e is not well reproduced in the current modeling with the three planets. This might suggest the presence of additional planets and/or minor bodies that have evaded the detection so far.

It is definitely premature to draw any decisive conclusions at this point. Nevertheless, the above possible discrepancies between the TTV and RV analyses point to the importance of future follow-up observations of the KOI-94 system.

In addition, we constructed an analytic model of the PPE. We derived a practical approximate formula that explicitly yields the difference between the longitudes of ascending nodes (mutual inclination in the plane of the sky) of the two planets in terms of the observed height,

central time, and duration of the brightening caused by the PPE. We showed that the PPE light curve observed in the KOI-94 system indeed gives a unique solution for the mutual inclination. The effect of the non-zero eccentricities is taken into account in the formulation described in Appendix C, though it is safely neglected for the KOI-94 system. Combining the TTV best-fit parameters and our analytic PPE model, the next PPE in this system is predicted to occur in the double transit around BJD = 2461132.4 (date in UT 2026 April 1/2). The occurrence of the next PPE is robust against the 1σ uncertainties of the parameters. Since the predicted height of the bump is much larger than the last one, the detection of this PPE is highly feasible. Indeed, the predicted height of the next PPE sensitively changes with the value of m_d . Thus the observation may be used to distinguish between the TTV and RV solutions.

This work is based on the photometry of KOI-94 provided by NASA's *Kepler* mission, and the authors express special thanks to the *Kepler* team. K.M. is supported by the Leading Graduate Course for Frontiers of Mathematical Sciences and Physics. The work by T.H. is supported by Japan Society for Promotion of Science (JSPS) Fellowship for Research (No. 25-3183). A.T. acknowledges the support from Grant-in-Aid for Scientific Research by JSPS (No. 24540257). M.N. is supported by Grant-in-Aid for Scientific Research on Innovative Areas (No. 23103005). Y.S. gratefully acknowledges the supports from the Global Collaborative Research Fund "A World-wide Investigation of Other Worlds" grant, the Global Scholars Program of Princeton University, and the Grant-in Aid for Scientific Research by JSPS (No. 24340035).

APPENDIX

OBSERVED TRANSIT TIMES OF KOI-94c, KOI-94d, AND KOI-94e

In Section 2, we fit each transit of KOI-94c, KOI-94d, and KOI-94e for the time of transit center, using the transit parameters in Table 3. The resulting transit times of the three planets, as well as their errors, χ^2 values, and deviations from the linear ephemerides in Table 4 are shown in Tables 8 to 10 in this Appendix.

ANALYSIS OF THE TTV OF KOI-94c USING ANALYTIC FORMULAE

Lithwick et al. (2012) derived analytic formulae for the TTV signals from two coplanar planets near a $j : j - 1$ mean motion resonance. Here we present a brief outline of their formulation and report the analysis of the TTVs of KOI-94c and KOI-94d using these formulae.

We let unprimed and primed symbols stand for the quantities associated with inner and outer planets, respectively. Then $\delta t \equiv (\text{observed } t_c) - (t_c \text{ calculated from linear ephemeris})$ for the inner and outer planets are given by

$$\delta t = |V| \sin(\lambda^j + \arg V), \quad \delta t' = |V'| \sin(\lambda^j + \arg V'), \quad (\text{B1})$$

where λ^j , V , and V' are defined as follows.

The longitude of conjunction λ^j is defined as

$$\lambda^j \equiv j\lambda' - (j - 1)\lambda, \quad (\text{B2})$$

where $\lambda' = 2\pi(t - T')/P'$ and $\lambda = 2\pi(t - T)/P$. If we measure angles with respect to the line of sight, T and T' are the times of any particular transits of the inner and outer planet, respectively. Here we choose T (T') to be t_0 (t'_0) in Table 4. Defining the super-period P^j and the normalized distance to resonance by

$$P^j \equiv \frac{1}{|j/P' - (j - 1)/P|} \quad (\text{B3})$$

and

$$\Delta \equiv \frac{P'}{P} \frac{j - 1}{j} - 1, \quad (\text{B4})$$

TABLE 8
 TRANSIT TIMES OF KOI-94c.

Transit number	t_c (BJD - 2454833)	$1\sigma_{\text{lower}}$	$1\sigma_{\text{upper}}$	$\chi^2/\text{d.o.f}$	$O - C$ (days)
21	356.90817	0.00102	0.00092	1.10	0.00245
22	367.33115	0.00110	0.00136	1.17	0.00174
23	377.75187	0.00142	0.00133	0.97	-0.00124
24	388.17539	0.00094	0.00086	1.15	-0.00140
26	409.02071	0.00231	0.00269	1.08	-0.00346
27	419.44211	0.00082	0.00085	1.02	-0.00575
28	429.86657	0.00197	0.00148	1.02	-0.00497
29	440.29072	0.00080	0.00087	1.24	-0.00452
30	450.71607	0.00120	0.00115	1.00	-0.00286
31	461.13894	0.00231	0.00170	1.10	-0.00368
32	471.56699	0.00124	0.00133	1.17	0.00069
33	481.99307	0.00072	0.00073	1.05	0.00308
34	492.41692	0.00116	0.00138	1.18	0.00324
35	502.84201	0.00107	0.00102	1.13	0.00464
36	513.26385	0.00101	0.00115	1.14	0.00279
37	523.68733	0.00101	0.00095	1.05	0.00259
38	534.10875	0.00100	0.00093	1.22	0.00032
58	742.57675	0.00088	0.00091	1.11	-0.00546
61	773.85373	0.00147	0.00122	1.17	0.00045
62	784.27831	0.00165	0.00115	1.17	0.00135
63	794.70489	0.00076	0.00085	1.13	0.00423
65	815.55087	0.00127	0.00128	1.10	0.00283
66	825.97556	0.00069	0.00072	0.94	0.00384
67	836.39887	0.00097	0.00114	1.01	0.00346
68	846.81847	0.00101	0.00126	1.13	-0.00063
69	857.24112	0.00111	0.00096	1.08	-0.00167
71	878.08547	0.00094	0.00089	1.09	-0.00469
72	888.51143	0.00146	0.00191	1.16	-0.00243
73	898.93547	0.00092	0.00087	1.07	-0.00207
93	1107.41537	0.00097	0.00127	1.01	0.00405
95	1128.26345	0.00112	0.00145	1.11	0.00475
96	1138.68565	0.00111	0.00091	1.06	0.00326
97	1149.10740	0.00118	0.00121	0.94	0.00133
98	1159.52802	0.00122	0.00116	1.02	-0.00174
99	1169.95296	0.00095	0.00108	1.10	-0.00049
100	1180.37319	0.00136	0.00161	1.00	-0.00395
101	1190.79857	0.00119	0.00116	1.14	-0.00226
102	1201.21882	0.00100	0.00119	1.19	-0.00570
103	1211.64373	0.00122	0.00119	1.06	-0.00448
104	1222.06922	0.00076	0.00073	1.17	-0.00268
105	1232.49526	0.00147	0.00137	1.29	-0.00032
106	1242.92076	0.00113	0.00132	0.96	0.00149
107	1253.34432	0.00091	0.00085	1.17	0.00136
108	1263.77117	0.00136	0.00095	1.17	0.00452

 TABLE 9
 TRANSIT TIMES OF KOI-94d.

Transit number	t_c (BJD - 2454833)	$1\sigma_{\text{lower}}$	$1\sigma_{\text{upper}}$	$\chi^2/\text{d.o.f}$	$O - C$ (days)
10	356.17032	0.00023	0.00023	1.10	-0.00041
11	378.51394 ^a	0.00023	0.00023	1.25	0.00023
13	423.19948	0.00023	0.00023	1.17	-0.00017
14	445.54263	0.00022	0.00023	1.14	0.00002
15	467.88668	0.00021	0.00022	1.06	0.00109
16	490.22897	0.00022	0.00022	1.07	0.00042
17	512.57051	0.00021	0.00021	1.17	-0.00101
18	534.91389	0.00022	0.00022	1.08	-0.00060
27	736.00250	0.00023	0.00023	1.00	0.00128
28	758.34519	0.00023	0.00023	1.10	0.00100
29	780.68635	0.00023	0.00023	1.13	-0.00080
31	825.37220	0.00022	0.00022	1.06	-0.00090
32	847.71579	0.00022	0.00022	1.14	-0.00028
33	870.05926	0.00026	0.00026	1.03	0.00022
34	892.40212	0.00022	0.00022	1.11	0.00011
44	1115.83180	0.00024	0.00024	2.02	0.00009
45	1138.17339	0.00023	0.00023	1.10	-0.00129
48	1205.20344	0.00023	0.00023	1.11	-0.00014
49	1227.54827	0.00022	0.00023	1.01	0.00172
50	1249.89001	0.00022	0.00022	1.08	0.00048
51	1272.23152	0.00022	0.00023	0.94	-0.00098

^aDouble transit with KOI-94e: obtained simultaneously with the relative nodal angle and t_c for KOI-94e.

TABLE 10
TRANSIT TIMES OF KOI-94e.

Transit number	t_c (BJD - 2454833)	$1\sigma_{\text{lower}}$	$1\sigma_{\text{upper}}$	$\chi^2/\text{d.o.f}$	$O - C$ (days)
4	378.51677 ^a	0.00056	0.00055	1.25	-0.00150
5	432.83744	0.00062	0.00063	1.22	-0.00068
6	487.15505	0.00060	0.00062	1.11	-0.00292
11	758.76221	0.00059	0.00060	0.98	0.00500
12	813.08158	0.00061	0.00061	1.10	0.00452
18	1138.99524	0.00060	0.00062	1.21	-0.00091
19	1193.31417	0.00062	0.00063	1.19	-0.00183
20	1247.63414	0.00060	0.00062	1.24	-0.00171

^aDouble transit with KOI-94d: obtained simultaneously with the relative nodal angle and t_c for KOI-94d.

λ^j can be written as

$$\begin{aligned}\lambda^j &= -2\pi \left(\frac{j-1}{P} - \frac{j}{P'} \right) t + 2\pi \left(\frac{(j-1)T}{P} - \frac{jT'}{P'} \right) \\ &= -\frac{\Delta}{|\Delta|} \frac{2\pi}{P^j} \left(t - \frac{(1+\Delta)T - T'}{\Delta} \right).\end{aligned}\quad (\text{B5})$$

Thus, if $\Delta > 0$, λ^j is retrograde with respect to the orbital motion and is prograde for $\Delta < 0$.

The complex TTV amplitudes V and V' are given by

$$V = P \frac{\mu'}{\pi j^{2/3} (j-1)^{1/3} \Delta} \left(-f - \frac{3}{2} \frac{Z_{\text{free}}^*}{\Delta} \right) \quad (\text{B6})$$

and

$$V' = P' \frac{\mu}{\pi j \Delta} \left(-g + \frac{3}{2} \frac{Z_{\text{free}}^*}{\Delta} \right), \quad (\text{B7})$$

where f and g are the sums of the Laplace coefficients given by

$$f = -1.190 + 2.20\Delta = -1.032 < 0, \quad g = 0.4284 - 3.69\Delta = 0.1637 > 0 \quad (\text{B8})$$

for $j = 2$, $\Delta = 0.07174$, and μ (μ') is the mass ratio of the inner (outer) planet to that of the star. They also introduce Z_{free} as a linear combination of the free complex eccentricities of the two planets

$$Z_{\text{free}} = f z_{\text{free}} + g z'_{\text{free}}, \quad (\text{B9})$$

where z_{free} is defined as the ‘‘free’’ part of the complex eccentricity

$$z \equiv e \exp(i\varpi), \quad (\text{B10})$$

and obtained by subtracting z_{forced} , the forced eccentricity due to the planet’s proximity to resonance, from z . The forced eccentricities for the inner and outer planets are

$$\begin{pmatrix} z_{\text{forced}} \\ z'_{\text{forced}} \end{pmatrix} = -\frac{1}{j\Delta} \begin{pmatrix} \mu' f (P/P')^{1/3} \\ \mu g \end{pmatrix} e^{i\lambda^j}. \quad (\text{B11})$$

Since $\Delta \gtrsim 0.01$ and $\mu \lesssim 10^{-4}$ typically, $|z_{\text{forced}}| \lesssim 10^{-2}$, in which case

$$Z_{\text{free}} \simeq f e e^{i\varpi} + g e' e^{i\varpi'} = (f e \cos \varpi + g e' \cos \varpi') + i(f e \sin \varpi + g e' \sin \varpi'). \quad (\text{B12})$$

(Xie 2013). Note that in either the limit that $|Z_{\text{free}}| \ll |\Delta|$ or $|Z_{\text{free}}| \gg |\Delta|$, phases of the two planets’ TTVs are anti-correlated, as can be seen from the expressions for V and V' . In this case, TTV signals of the two planets provide only three independent quantities, making it impossible to uniquely determine $|V|$, $|V'|$, $\text{Re}(Z_{\text{free}})$, and $\text{Im}(Z_{\text{free}})$.

Above expressions for V and V' imply that the phases as well as the amplitudes of the two TTV signals contain important information about their eccentricities. For ease of discussion, they define

$$\phi_{\text{ttv}} \equiv \arg \left(V \times \frac{\Delta}{|\Delta|} \right), \quad \phi'_{\text{ttv}} \equiv \arg \left(V' \times \frac{\Delta}{|\Delta|} \right). \quad (\text{B13})$$

With these definitions, $Z_{\text{free}} = 0$ leads to $\phi_{\text{ttv}} = 0$ deg and $\phi'_{\text{ttv}} = 180$ deg, independently of the sign of Δ . In this case, since λ^j decreases (increases) with time for $\Delta > 0$ ($\Delta < 0$), δt crosses zero from above (below) whenever $\lambda^j = 0$. If the observed TTVs have a phase shift with respect to $\phi_{\text{ttv}} = 0$ deg and $\phi'_{\text{ttv}} = 180$ deg, this implies that non-zero Z_{free} exists. On the other hand, no phase shift does not necessarily mean $Z_{\text{free}} = 0$, for the phase of Z_{free} may vanish by chance. Although it is impossible to judge whether Z_{free} is really zero or not in a single resonant pair with no phase shift, important conclusions can be obtained by statistical analyses (Wu & Lithwick 2013).

TABLE 11
 COMPLEX TTVs FOR KOI-94c AND KOI-94d.

Δ	$ V_c $ (days)	$\phi_{\text{ttv},c}$ (deg)	$ V_d $ (days)	$\phi_{\text{ttv},d}$ (deg)	$\chi_c^2/\text{d.o.f}$	$\chi_d^2/\text{d.o.f}$
0.07174	0.0045 ± 0.0003	38 ± 3	0.00081 ± 0.00020	253 ± 16	0.85	8.6

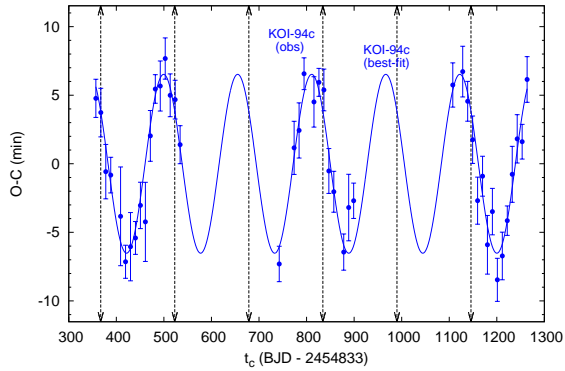


FIG. 16.— Best-fit theoretical TTV (solid line) for the observed transit times of KOI-94c based on Eq.(B1) by Lithwick et al. (2012). Points with error bars are the observed TTVs of KOI-94c calculated with t_0 and P obtained from the fit including TTVs (see Eq.(B14)). Vertical arrows show the times at which $\lambda_j = 0$, i.e., the longitude of conjunction points to the observer. The observed phase of the TTV is slightly shifted from these points, suggesting small but nonzero eccentricities.

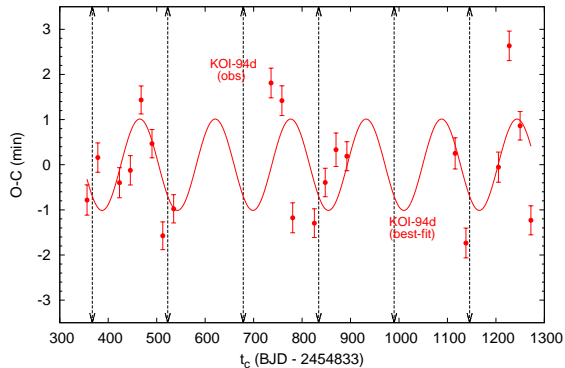


FIG. 17.— Best-fit theoretical TTV (solid line) for the observed transit times of KOI-94d based on Eq.(B1) by Lithwick et al. (2012) (same as Figure 16).

Based on the formulation above, the transit times t_{trans} for the inner planet are written as

$$t_{\text{trans}} = t_0 + P i_{\text{trans}} + \text{Re}(V) \sin \lambda^j + \text{Im}(V) \cos \lambda^j, \quad (\text{B14})$$

where $i_{\text{trans}} = 0, 1, \dots$ is the transit number. For each observed t_{trans} , we calculate λ^j using P and t_0 obtained by a linear fit (Table 4), and fit for the four parameters t_0 , P , $\text{Re}(V)$, and $\text{Im}(V)$ by a least-square fit. We also repeat the same procedure for the outer planet, and obtain the results in Table 11. The best-fit theoretical curve in Figure 16 shows that the TTV of KOI-94c is well explained only by the effect from KOI-94d, having the same period as expected from their proximity to 2:1 resonance. In contrast, the TTV of KOI-94d is poorly explained by the contribution from KOI-94c alone (Figure 17). These results are consistent with our estimates in Table 5.

TTV amplitudes listed in Table 11 give estimates for the masses of KOI-94d and KOI-94c. If we assume $Z_{\text{free}} = 0$, i.e., that both of the planets have zero eccentricities, Eq.(B6) translates the amplitude of KOI-94c's TTV $|V_c|$ into the nominal mass $m_d = 63M_{\oplus}$.¹⁴ However, the accuracy of this estimate is rather limited, because the slight phase shift in KOI-94c's TTV suggests that KOI-94d and/or KOI-94c have small but nonzero eccentricities. If this nominal mass is actually close to the true one, the density of KOI-94d is $\sim 0.3 \text{ g cm}^{-3}$, which is comparable to that of the lowest-density exoplanet ever discovered.

¹⁴ $|V_d|$ corresponds to a comparatively large nominal mass $m_c = 36M_{\oplus}$, but this value includes the contributions both from KOI-94c and KOI-94e.

$\mathcal{O}(e)$ FORMULATION OF THE PPE

In Section 3, we modeled the PPE caused by two planets on circular orbits. Here we summarize how the $\mathcal{O}(e)$ correction modifies those results.

In the presence of a nonzero eccentricity, the sky-plane distance between the star and planet r_{sky} is given by

$$r_{\text{sky}} = \frac{a(1-e^2)}{1+e\cos f} \sqrt{1 - \sin^2(\omega+f)\sin^2 i}. \quad (\text{C1})$$

Defining $\Delta \equiv \frac{\pi}{2} - (\omega+f)$, Δ that minimizes this r_{sky} satisfies

$$\Delta = \frac{1}{2} \arcsin \left[2e \cos(\omega+\Delta) \left(\frac{1}{\sin^2 i} - \cos^2 \Delta \right) - e \sin(\omega+\Delta) \sin 2\Delta \right], \quad (\text{C2})$$

which can be solved to the leading orders of e and $\pi/2 - i$ to give

$$\Delta \simeq e \cos \omega \left(\frac{\pi}{2} - i \right)^2 \sim e \cos \varpi \left(\frac{a}{R_\star} \right)^{-2}. \quad (\text{C3})$$

Thus, the impact parameter b can be approximated as

$$b \simeq \frac{a \cos i}{R_\star} \cdot \frac{1-e^2}{1+e\sin\omega} \simeq \frac{a \cos i}{R_\star} (1-e\sin\omega) \quad (\text{C4})$$

(Winn 2010). This alters the expression (12) as

$$\mathbf{r}_j \simeq (1 - e_j \cos f_j) \begin{pmatrix} (a_j/R_\star) \cos \Omega_j \cos(\omega_j + f_j) - b_j(1 + e_j \sin \omega_j) \sin \Omega_j \sin(\omega_j + f_j) \\ (a_j/R_\star) \sin \Omega_j \cos(\omega_j + f_j) + b_j(1 + e_j \sin \omega_j) \cos \Omega_j \sin(\omega_j + f_j) \end{pmatrix}. \quad (\text{C5})$$

In addition, the expansion of $\omega+f$ around t_c is modified as

$$\omega+f \simeq \frac{\pi}{2} + n(1+2e\sin\omega)(t-t_c). \quad (\text{C6})$$

Using these expressions, \mathbf{r}_j ($j=1,2$) can be expanded as

$$\mathbf{r}_j = \mathbf{v}_j \left[(1 + e_j \sin \omega_j)(t - t_c^{(j)}) \right] + \mathbf{r}_0^{(j)}, \quad (\text{C7})$$

where \mathbf{v}_j and $\mathbf{r}_0^{(j)}$ are the same as defined in Eq.(16). Accordingly, the expression for d with $\mathcal{O}(e)$ terms included is obtained by replacing b_j and n_j in the circular case with $b_j(1 - e_j \sin \omega_j)$ and $n_j(1 + e_j \sin \omega_j)$, respectively.

REFERENCES

- Agol, E., Steffen, J., Sari, R., & Clarkson, W. 2005, MNRAS, 359, 567
- Albrecht, S., Winn, J. N., Marcy, G. W., Howard, A. W., Isaacson, H., & Johnson, J. A. 2013, ApJ, 771, 11
- Batalha, N. M., et al. 2013, ApJS, 204, 24
- Bate, M. R., Lodato, G., & Pringle, J. E. 2010, MNRAS, 401, 1505
- Batygin, K. 2012, Nature, 491, 418
- Borucki, W. J., et al. 2011, ApJ, 736, 19
- Fabrycky, D. C. 2010, ArXiv e-prints
- Fabrycky, D. C., & Winn, J. N. 2009, ApJ, 696, 1230
- Fabrycky, D. C., et al. 2012, ApJ, 750, 114
- Goldreich, P., & Tremaine, S. 1980, ApJ, 241, 425
- Hirano, T., Suto, Y., Winn, J. N., Taruya, A., Narita, N., Albrecht, S., & Sato, B. 2011, ApJ, 742, 69
- Hirano, T., et al. 2012, ApJ, 759, L36
- Holman, M. J., & Murray, N. W. 2005, Science, 307, 1288
- Kinemuchi, K., Barclay, T., Fanelli, M., Pepper, J., Still, M., & Howell, S. B. 2012, PASP, 124, 963
- Kokubo, E., & Makino, J. 2004, PASJ, 56, 861
- Lai, D., Foucart, F., & Lin, D. N. C. 2011, MNRAS, 412, 2790
- Lissauer, J. J., et al. 2011, Nature, 470, 53
- Lithwick, Y., Xie, J., & Wu, Y. 2012, ApJ, 761, 122
- Lubow, S. H., & Ida, S. 2011, Planet Migration, ed. S. Seager, 347–371
- Mandel, K., & Agol, E. 2002, ApJ, 580, L171
- Markwardt, C. B. 2009, in Astronomical Society of the Pacific Conference Series, Vol. 411, Astronomical Data Analysis Software and Systems XVIII, ed. D. A. Bohlender, D. Durand, & P. Dowler, 251
- McLaughlin, D. B. 1924, ApJ, 60, 22
- Nagasawa, M., Ida, S., & Bessho, T. 2008, ApJ, 678, 498
- Naoz, S., Farr, W. M., Lithwick, Y., Rasio, F. A., & Teyssandier, J. 2011, Nature, 473, 187
- Nesvorný, D., Kipping, D. M., Buchhave, L. A., Bakos, G. Á., Hartman, J., & Schmitt, A. R. 2012, Science, 336, 1133
- Ohta, Y., Taruya, A., & Suto, Y. 2005, ApJ, 622, 1118
- . 2009, ApJ, 690, 1
- Queloz, D., Eggenberger, A., Mayor, M., Perrier, C., Beuzit, J. L., Naef, D., Sivan, J. P., & Udry, S. 2000, A&A, 359, L13
- Rabus, M., et al. 2009, A&A, 494, 391
- Ragozzine, D., & Holman, M. J. 2010, ArXiv e-prints
- Rogers, T. M., Lin, D. N. C., & Lau, H. H. B. 2012, ApJ, 758, L6
- Rossiter, R. A. 1924, ApJ, 60, 15
- Seager, S., & Mallén-Ornelas, G. 2003, ApJ, 585, 1038
- Torres, G., Fischer, D. A., Sozzetti, A., Buchhave, L. A., Winn, J. N., Holman, M. J., & Carter, J. A. 2012, ApJ, 757, 161
- Valenti, J. A., & Piskunov, N. 1996, A&AS, 118, 595
- Weiss, L. M., et al. 2013, ApJ, 768, 14
- Winn, J. N. 2010, ArXiv e-prints
- Winn, J. N., et al. 2005, ApJ, 631, 1215
- Wu, Y., & Lithwick, Y. 2011, ApJ, 735, 109
- . 2013, ApJ, 772, 74
- Wu, Y., & Murray, N. 2003, ApJ, 589, 605
- Xie, J.-W. 2013, ApJS, 208, 22
- Xie, J.-W., Wu, Y., & Lithwick, Y. 2013, ArXiv e-prints